

Mesh refinement and modelling errors in flow simulation

Antony Jameson
Princeton Univ., NJ

Luigi Martinelli
Princeton Univ., NJ

AIAA, Fluid Dynamics Conference, 27th, New Orleans, LA, June 17-20, 1996

We present a perspective on verification and validation of CFD tools for analysis and design, identifying principal sources of error due to approximations in the physical model, numerical discretization, and implementation. Issues in algorithm design and trade-offs between modelling accuracy and computational costs are discussed in detail. Computational examples are drawn from the authors work in several applications areas. (Author)

Mesh Refinement and Modelling Errors in Flow Simulation

Antony Jameson[†] and Luigi Martinelli[‡]
Department of Mechanical and Aerospace Engineering
Princeton University
Princeton, New Jersey 08544 USA

ABSTRACT

This paper presents a perspective on verification and validation of computational fluid dynamics tools for analysis and design. It identifies principal sources of error due to approximations in the physical model, numerical discretization, and implementation. Issues in algorithm design and trade-offs between modelling accuracy and computational costs are discussed in detail. Computational examples are drawn from the authors work in several applications areas.

1. INTRODUCTION

The simulation of fluid flow involves two essential steps: (1) the definition of a suitable mathematical model which describes the physical system of interest, (2) the development and implementation of numerical techniques to compute a solution of the mathematical model using digital computers. Both steps generally introduce approximation in the simulation, and the resulting errors should be understood and possibly quantified. Thus, both the mathematical model and the numerical method need to be verified and validated.

While in the literature there is a general agreement on the logical steps that must be taken to validate a complex numerical method, it is almost impossible to find a precise definition of the terms verification and validation. Golub and Ortega [14] give the following definition of Validation: "... validation of the model. By this we mean a verification that the solution we compute is sufficiently accurate to serve the purpose for which the model was constructed." This is a very elegant and precise definition, but it only identifies validation of the entire solution process. Through this paper, in defining validation and verification we take a rather classical view in which verification is needed for every single claim made in constructing the model, or submodels, (both physi-

cal, and numerical), whereas validation is intended to show the general validity (or failure) of the overall approach, or submodel, by comparisons with independent empirical, analytical, or numerical observations. In our definition, the distinction between verification and validation is clearly demarked and consistent with their etymology. Validation refers to a successful comparison of the models (or submodels) with *independent* observations. Verification of the mathematical model means proving that its logical derivation is correct, and that it is consistent with general physical principles (e.g. Galilean invariance). To make the distinction between the two terms more clear, in our mind a statement such as "the Euler equations represent a good model for the simulation of cruise conditions" requires logical verification by showing for example that in the limit of large Reynolds number the equations of motion of a fluid approach the Euler equations. On the other hand, validation of the Euler equations as a suitable mathematical model for cruise requires agreement of the prediction obtained using such a model with independent empirical observation such as experimental data at high Reynolds numbers. Thus, similar to the validation of any scientific theory, the validation of a mathematical model may involve testing its predictions with new experiments, as in the example of the gravitational bending of light rays which was used to validate general relativity.

In the context of fluid dynamics, mostly due to the mathematical complexity of the equations used to describe the flow and the lack of analytic solutions, the validation of the physical model relies on numerical computations. This poses additional difficulties unless the numerical solution process has been separately verified and validated.

For a numerical method, internal and logical verification require proof that discretization and round off errors can be bounded and that, in principle, the numerical method will compute an accurate solution of the mathematical model with small enough mesh width, and sufficient precision. For example, we may prove that the error approaches zero as some power of the mesh width assuming exact arithmetic, and we may also verify this by numerical experiments.

Copyright ©1996 by the Authors. Published by the AIAA Inc. with permission

†James S. McDonnell Distinguished University Professor of Aerospace Engineering, AIAA Fellow

‡Assistant Professor, AIAA Member

Validation of the numerical method means confirmation that the actual implementation in software converges to a correct answer when the mesh width and the time step are sufficiently small. A correct answer may be supplied as independent solutions of the model, either analytical (for special cases) or by independently developed numerical methods. Thus, a direct comparison of the numerical results with both analytical solutions and independent numerical results may be used to validate the numerical solution process.

For a properly posed initial value problem, classical numerical analysis techniques can be used for verification (including both consistency and proof of convergence) of a numerical method. However, the non-linearity of the conservation laws, and the geometric complexity of the flow domain of interest in most applications, make it difficult to devise elegant analytical tools for the verification of a numerical scheme. Thus, although algorithms have been the subject of intensive development for the past two decades, and the principles underlying the design and implementation of robust schemes which can accurately resolve the inviscid conservation laws for compressible flows are now quite well established, mesh refinement remains the most obvious and successful technique available for final verification. It allows us to verify both the level of accuracy of the scheme and the correctness of the implementation on a computer, which often require many thousand lines of code. For example, careful mesh refinement studies for boundary layer flow have proven to be essential in the verification of a class of finite volume based schemes [40, 41] which are currently employed in a wide range of applications. For time-resolved calculations a similar verification study should be performed by computing with a sequence of time steps to infer the level of time-accuracy of the calculations.

Despite the advances that have been made, CFD methods for high Reynolds number viscous flow are still not validated as one would like before their use in the design process. The fidelity of modelling of high Reynolds number viscous flows continues to be limited by computational costs, and, for separated flows, by inadequate turbulence modeling. In this case the validation of the mathematical model and of the numerical method are not entirely independent processes. And care must be taken to isolate the cause of discrepancy either in the mathematical model, or in the numerical scheme. Grid refinement studies are, once again, instrumental for eliminating uncertainties and errors attributable to the numerical scheme.

Once the mathematical model and the numerical solution procedure have been verified and validated, the final validation of the simulation process can be

carried out by comparing the results predicted by the simulation with independent empirical data.

A critical issue, examined in the next Section, is the choice and the verification of mathematical models. What level of complexity is needed to provide sufficient accuracy for a given fluid problem, and what is the impact on the validation of the whole simulation? Section 3 addresses the verification and validation of numerical algorithms for flow simulations by discussing examples drawn from the authors' work in several applications areas.

2. VERIFICATION AND VALIDATION OF MATHEMATICAL MODELLING

The choice of an appropriate mathematical model represents a trade-off between the accuracy required in the simulation and the computational complexity and cost. Non-linearities, and a disparity of length and time scales control many critical phenomena of fluid flow. For example, while the actual thickness of a shock wave is of the order of a mean free path of the gas particles, on a macroscopic scale its thickness is essentially zero. In turbulent flow energy is transferred from large scale motions to progressively smaller eddies until the scale becomes so small that the motion is dissipated by viscosity. The ratio of the length scale of the global flow to that of the smallest persisting eddies is of the order $Re^{\frac{2}{3}}$, where Re is the Reynolds number, typically in the range of 30 million for an aircraft, and even larger for naval applications. In order to resolve such scales in all three space directions a computational grid with the order of $Re^{\frac{2}{3}}$ cells would be required. This is beyond the range of any current or foreseeable computer. Consequently mathematical models with varying degrees of simplification have to be introduced in order to make computational simulation of flow feasible and produce viable and cost-effective methods.

Figure 1 (supplied by Pradeep Raj) indicates a hierarchy of models at different levels of simplification which have proved useful in aeronautics. Efficient flight is generally achieved by the use of smooth and streamlined shapes which avoid flow separation and minimize viscous effects, with the consequence that useful predictions can be made using inviscid models. The elimination of viscous effects allows the assumption of irrotational flow which leads to Laplace's equation for incompressible flow, and the linearized supersonic flow equation for high speed flow past slender bodies. While simplified models of this type can be very useful in applications which are close to satisfying the underlying assumptions, they are completely invalid for complex viscous flows. At an intermediate level of complexity are the non-linear inviscid models, including the transonic po-

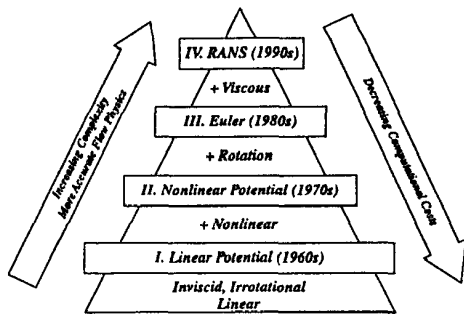


Figure 1: Hierarchy of Fluid Flow Models

tential flow equation and the Euler equations.

The logical verification of these simplified models belongs to the field of classical fluid-dynamics. They have been extensively used in aircraft design and thus validated by several independent studies. However, the full viscous equations are likely to be needed for the simulation of arbitrary complex separated flows, which occur in several practical devices. High angle of attack aircraft, high lifting devices, multistage compressors and turbines, maneuvering submarines and ships. In order to treat these kinds of flow at high Reynolds numbers, one is generally forced to estimate turbulent effects by Reynolds averaging of the fluctuating components. This requires the introduction of a turbulence model.

It is doubtful whether a universally valid turbulence model, capable of describing all complex flows, could be devised [16]. Algebraic models [8, 3] have proved fairly satisfactory for the calculation of attached and slightly separated wing flows. These models rely on the thin layer approximation and usually incorporate separate formulas for the inner and outer layers, and they require an estimate of a length scale which depends on the thickness of the boundary layer. The estimation of this quantity by a search for a maximum of the vorticity times a distance to the wall, as in the Baldwin-Lomax model, can lead to ambiguities in internal flows, and also in complex vortical flows over slender bodies and highly swept or delta wings [12, 28]. The Johnson-King model [22], which allows for non-equilibrium effects through the introduction of an ordinary differential equation for the maximum shear stress, has improved the prediction of flows with shock induced separation [34, 24].

Closure models depending on the solution of transport equations are widely accepted for industrial applications. These models eliminate the need to estimate a length scale by detecting the edge of the boundary layer. Eddy viscosity models typically use two equations for the turbulent kinetic energy k and the dissipation rate ϵ , or a pair of equivalent quantities [23, 42, 39, 1, 29, 10]. Models of this type

generally tend to present difficulties in the region very close to the wall. They also tend to be badly conditioned for numerical solution. The $k-l$ model [36] is designed to alleviate this problem by taking advantage of the linear behaviour of the length scale l near the wall. In an alternative approach to the design of models which are more amenable to numerical solution, new models requiring the solution of one transport equation have recently been introduced [4, 38]. The performance of the algebraic models remains competitive for wing flows, but the one- and two-equation models show promise for broader classes of flows. In order to achieve greater universality, research is also being pursued on more complex Reynolds stress transport models, which require the solution of a larger number of transport equations.

Unfortunately, the mathematical complexity of the most advanced turbulence models does not, in general, allow for the analytical verification of the models. Thus, verification of the physical submodel becomes dependent on the technique which is selected to numerically solve the turbulence model equations. For this reason, a direction of research which attempts to devise more rational models via renormalization group (RNG) theory [45, 37] is particularly appealing. With more traditional turbulence models, it becomes crucial that the validation of the turbulence model is carried out by comparing grid-independent solutions to experimental data other than the one which are used to calibrate the empirical constants of the model. Unfortunately, because of the costs associated with three dimensional RANS simulations, this is seldom possible, but with the advent of even faster computers this should become common practice in the verification and validation of turbulence models.

The selection of sufficiently accurate mathematical models and a judgment of their cost effectiveness ultimately rests with industry. Aircraft and spacecraft designs normally pass through the three phases of conceptual design, preliminary design, and detailed design. Correspondingly, the appropriate CFD models will vary in complexity. In the conceptual and preliminary design phases, the emphasis will be on relatively simple models which can give results with very rapid turn-around and low computer costs, in order to evaluate alternative configurations and perform quick parametric studies. The detailed design stage requires the most complete simulation that can be achieved with acceptable cost.

3. VERIFICATION AND VALIDATION OF CFD ALGORITHMS

This section presents a series of examples of verification and validation in ascending order of complexity.

Section 3.1 considers steady inviscid flow in one, two and three dimensions, culminating in comparisons with experimental data which validate the applicability of the three dimensional Euler equations as a model suitable for attached flows over transonic and supersonic aircraft. Section 3.2 considers steady viscous flows, ranging from laminar boundary layers to turbulent flow over a delta wing. Unsteady incompressible inviscid flows are discussed in Section 3.3, and finally Section 3.4 presents an example of three dimensional unsteady viscous flow. The examples are designed to illustrate a systematic approach, proceeding from the verification of the correctness of the numerical scheme for representative flows to final validation of both the mathematical model and the complete software by comparison with experimental data.

3.1 Inviscid Flow Discretizations

3.1.1 One dimensional shock

As a first example of verification of a numerical scheme we consider the case of shock capturing in one dimensional flow. A theory describing the discrete shock structure of a variety of schemes which introduce upwind biasing by matrix diffusion has been developed by Jameson [19, 20]. These include the E-Characteristic scheme, which is equivalent to Roe's flux difference splitting [32], the H-characteristic scheme which exactly preserves constant total enthalpy in steady flow, and the E and H-CUSP schemes. The SLIP Construction [19] provides a way to preserve the same discrete shock structure in higher order schemes.

In order to verify the discrete structure of stationary shocks with the various schemes, calculations were performed for a one dimensional problem with initial data containing left and right states compatible with the Rankine-Hugoniot conditions. An intermediate state consisting of the arithmetic average of the left and right states was introduced at a single cell in the center of the domain. With this intermediate state the system is not in equilibrium, and the time dependent equations were solved to find an equilibrium solution with a stationary shock wave separating the left and right states. Table 1 shows the results for a shock wave at Mach 20 for the H-CUSP scheme. The SLIP construction was used with a soft limiter. The table shows the values of ρ , u , p , M and the entropy $S = \log \frac{p}{\rho^\gamma} - \log \left(\frac{p}{\rho^L} \right)$. The scheme displays a perfect one point shock structure. The entropy is zero to 4 decimal places upstream of the shock, and is constant to 4 decimal places downstream of the shock. There is a slight excursion of the entropy at the interior point in the results for the H-characteristic and H-CUSP schemes. The table also

verifies that the SLIP construction produces solutions which are entirely devoid of oscillations both upstream and downstream of the shock wave, and that it does not spread out the shock structure at all.

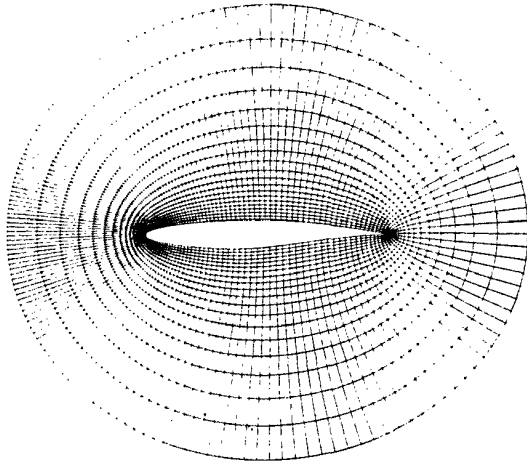
I	ρ	u	p	M	s
12	1.0000	23.6643	1.0000	20.0000	0.0000
13	1.0000	23.6643	1.0000	20.0000	0.0000
14	1.0000	23.6643	1.0000	20.0000	0.0000
15	1.0000	23.6643	1.0000	20.0000	0.0000
16	1.0000	23.6643	1.0000	20.0000	0.0000
17	1.0000	23.6643	1.0000	20.0000	0.0000
18	1.0000	23.6643	1.0000	20.0000	0.0000
19	1.0000	23.6643	1.0000	20.0000	0.0000
20	1.0000	23.6643	1.0000	20.0000	0.0000
21	1.0000	23.6643	1.0000	20.0000	0.0000
22	4.1924	7.3248	307.4467	0.7229	40.3353
23	5.9259	3.9935	466.4889	0.3804	37.6355
24	5.9259	3.9935	466.4889	0.3804	37.6355
25	5.9259	3.9935	466.4889	0.3804	37.6355
26	5.9259	3.9935	466.4889	0.3804	37.6355
27	5.9259	3.9935	466.4889	0.3804	37.6355
28	5.9259	3.9935	466.4889	0.3804	37.6355
29	5.9259	3.9935	466.4889	0.3804	37.6355
30	5.9259	3.9935	466.4889	0.3804	37.6355
31	5.9259	3.9935	466.4889	0.3804	37.6355
32	5.9259	3.9935	466.4889	0.3804	37.6355

Table 1: Shock Wave at Mach 20: H-CUSP scheme

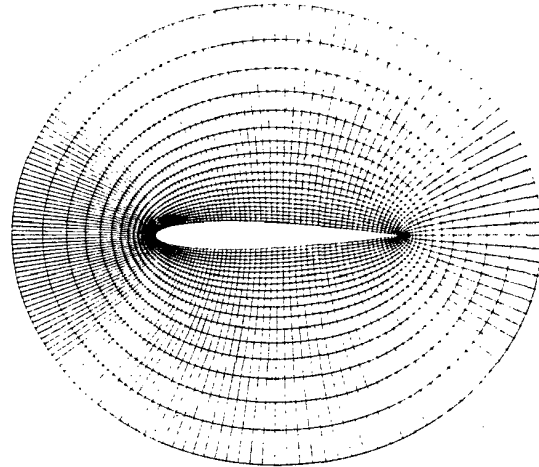
3.1.2 Airfoil calculations

The results of transonic flow calculations using the H-CUSP scheme are illustrated in figures (2-??). The final stagnation enthalpy is exactly constant, in accordance with the theory. The H-CUSP scheme was simplified by replacing the Roe averages by arithmetic averages.

Calculations are presented for two well known airfoils, the RAE 2822 and the NACA 0012. The equations were discretized on meshes with O-topology extending out to a radius of about 100 chords. In each case the calculations were performed on a sequence of successively finer meshes from 40x8 to 320x64 cells, while the multigrid cycles on each of these meshes descended to a coarsest mesh of 10x2 cells. Figure 2 shows the inner parts of the 160x32 meshes for the two airfoils. Figures 3-5 show the final results for each scheme on 320x64 meshes for the RAE 2822 airfoil at Mach .75 and 3° angle of attack, and for the NACA 0012 airfoil at Mach .8 and 1.25° angle of attack, and also at Mach .85 and 1° angle of attack. The convergence history is shown for 100 or 200 cycles, while the pressure distribution is displayed after a sufficient number of cycles for its convergence. The extended convergence histories provide a verification that the solution process will reach a true steady state, with residual errors that can be reduced to machine zero within round-off error, if it is continued for a sufficient number of cycles.

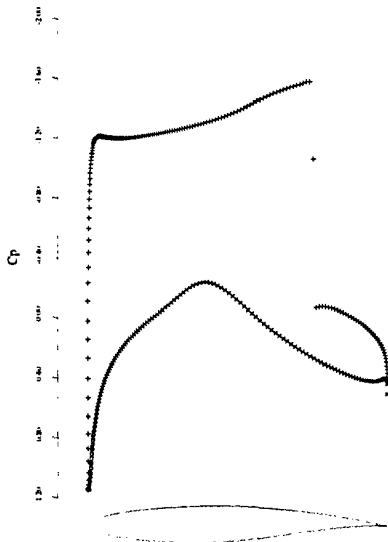


2a: RAE-2822 Airfoil

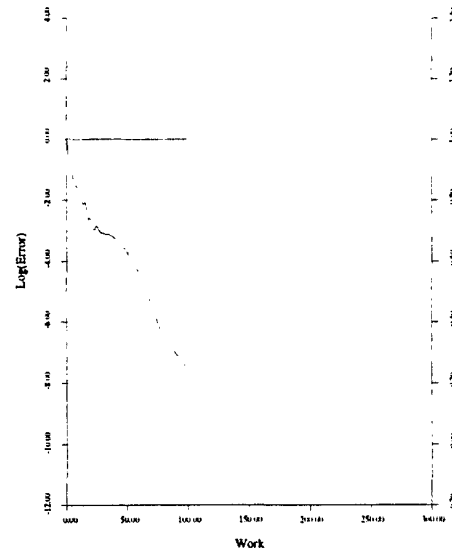


2b: NACA-0012 Airfoil

Figure 2: O-Topology Meshes, 160x32

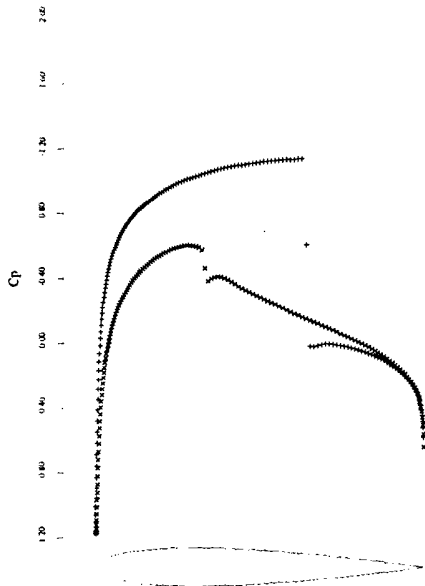


3a: C_p after 25 Cycles.
 $C_l = 1.1312$, $C_d = 0.0469$.

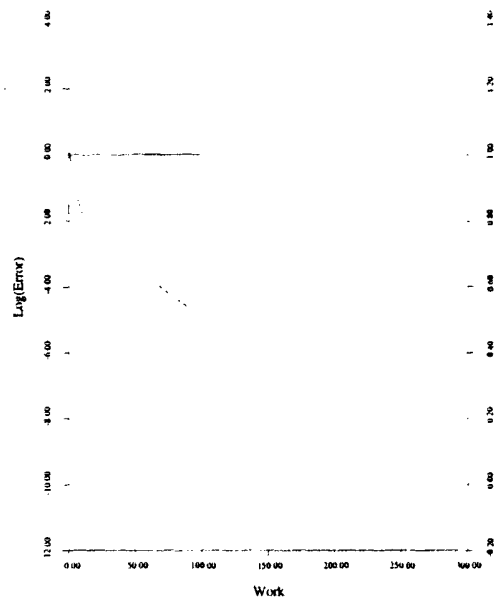


3b: Convergence.

Figure 3: RAE-2822 Airfoil at Mach 0.750 and $\alpha = 3.0^\circ$ H-CUSP Scheme.

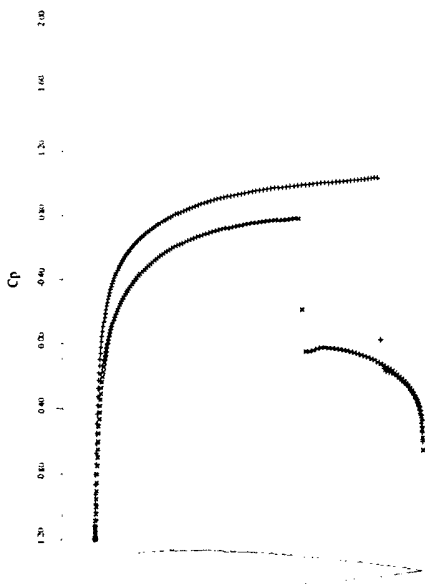


4a: C_p after 35 Cycles.
 $C_l = 0.3654$, $C_d = 0.0232$.

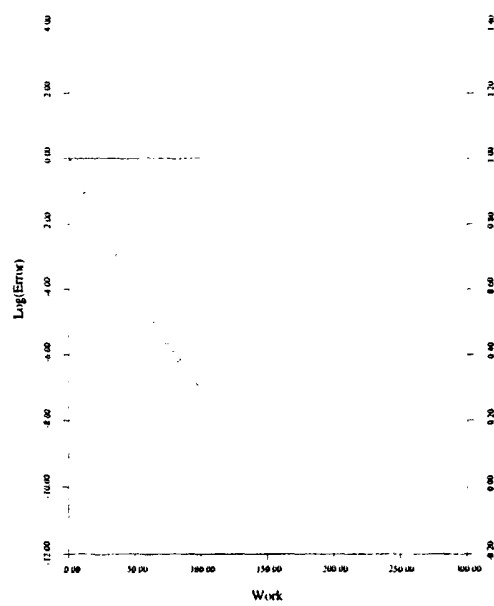


4b: Convergence.

Figure 4: NACA-0012 Airfoil at Mach 0.800 and $\alpha = 1.25^\circ$ H-CUSP Scheme.

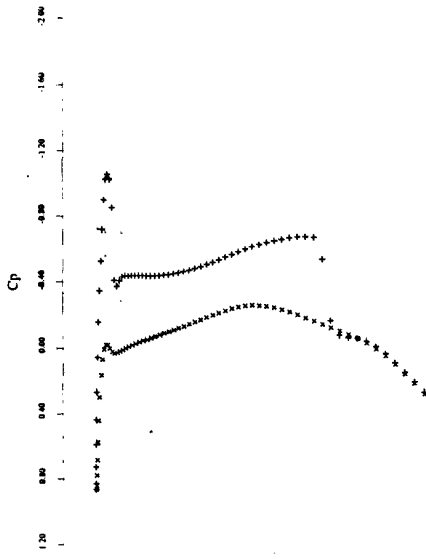


5a: C_p after 35 Cycles.
 $C_l = 0.3861$, $C_d = 0.0582$.

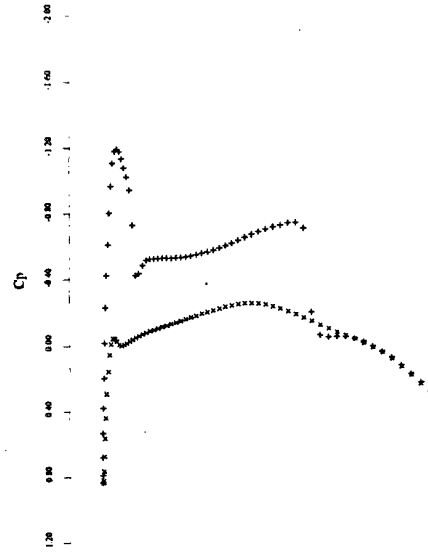


5b: Convergence.

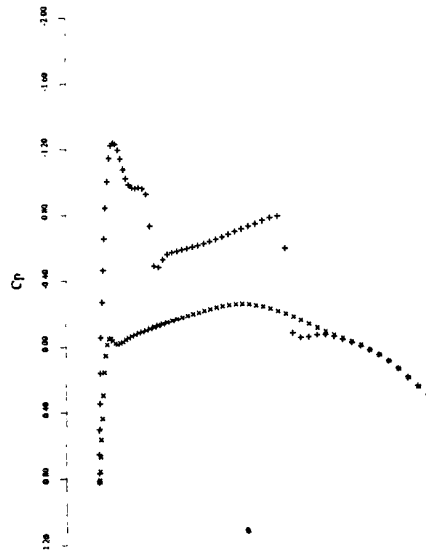
Figure 5: NACA-0012 Airfoil at Mach 0.850 and $\alpha = 1.0^\circ$ H-CUSP Scheme.



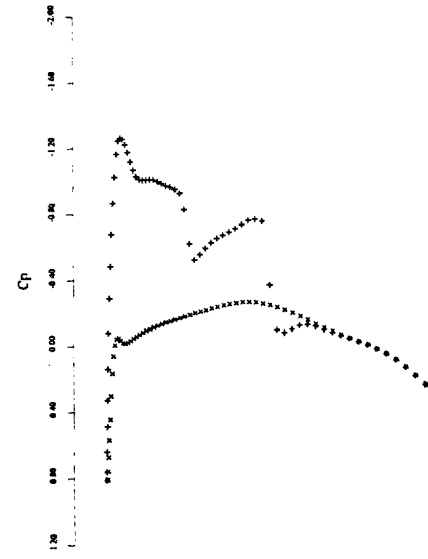
6a: 12.50% Span.
 $C_l = 0.2933$, $C_d = 0.0274$.



6b: 31.25% Span.
 $C_l = 0.3139$, $C_d = 0.0159$.



6c: 50.00% Span.
 $C_l = 0.3262$, $C_d = 0.0089$.



6d: 68.75% Span.
 $C_l = 0.3195$, $C_d = 0.0026$.

Figure 6: Onera M6 Wing. Mach 0.840, Angle of Attack 3.06°, 192×32×48 Mesh. $C_L = 0.3041$, $C_D = 0.0131$. H-CUSP scheme.

In the pressure distributions the pressure coefficient $C_p = \frac{p-p_\infty}{\frac{1}{2}\rho_\infty q_\infty^2}$ is plotted with the negative (suction) pressures upward, so that the upper curve represents the flow over the upper side of a lifting airfoil. The convergence histories show the mean rate of change of the density, and also the total number of supersonic points in the flow, which is almost immediately frozen in these calculations. The pressure distribution of the RAE 2822 airfoil converged in only 25 cycles. Convergence was slower for the NACA 0012 airfoil. In the case of flow at Mach .8 and 1.25° angle of attack, additional cycles were needed to damp out a wave downstream of the weak shock wave on the lower surface.

As a further check and verification of accuracy the drag coefficient should be zero in subsonic flow, or in shock free transonic flow. Table 2 shows the computed drag coefficient with the H-CUSP schemes on a sequence of three meshes for three examples. The first two are subsonic flows over the RAE 2822 and NACA 0012 airfoils at Mach .5 and 3° angle of attack. The third is the flow over the shock free Korn airfoil at its design point of Mach .75 and 0° angle of attack. In all three cases the drag coefficient is calculated to be zero to four digits on a 160x32 mesh. In aeronautical applications the accurate prediction of drag is particularly important, and an error as large as .0005 is significant since the total drag coefficient of the wing of a transport aircraft (including friction, vortex and shock drag) is in the range of .0150.

Mesh	RAE 2822 Mach .50 α 3°	NACA 0012 Mach .50 α 3°	Korn Airfoil Mach .75 α 0°
40x8	.0062	.0047	.0098
80x16	.0013	.0008	.0017
160x32	.0000	.0000	.0000

Table 2: Drag Coefficient on a sequence of meshes: H-CUSP scheme

3.1.3 Three-dimensional calculations for a swept wing

As a further verification of the performance of the H-CUSP scheme, the flow past the ONERA M6 wing was calculated on a mesh with C-H topology and 192x32x48 = 294912 cells. Figure 6 shows the result at Mach .84 and 3.06° angle of attack. This verifies that the non-oscillatory character of the solution is preserved in three-dimensions together with the sharp resolution of shock waves.

3.1.4 Validation of Euler Methods

In this section we present examples of three dimensional calculations which validate the use of the Eu-

ler equations in applications to real aircraft for which the flow remains attached, or else separation is fixed by sharp edges. Figure 7 shows a calculation of the Northrop YF23 by R.J. Busch, Jr., who used the Jameson's FLO57 code to solve the Euler equations [7]. Although an inviscid model of the flow was used, it can be seen that the simulations are in good agreement with wind tunnel measurements both at Mach .90, with angles of attack of 0, 8 and 16 degrees, and at Mach 1.5 with angles of attack of 0, 4 and 8 degrees. At a high angle of attack the flow separates from the leading edge, and this example shows that in situations where the point of separation is fixed, an inviscid model may still produce a useful prediction. Thus valuable information for the aerodynamic design could be obtained with a relatively inexpensive computational model. The next figures show the

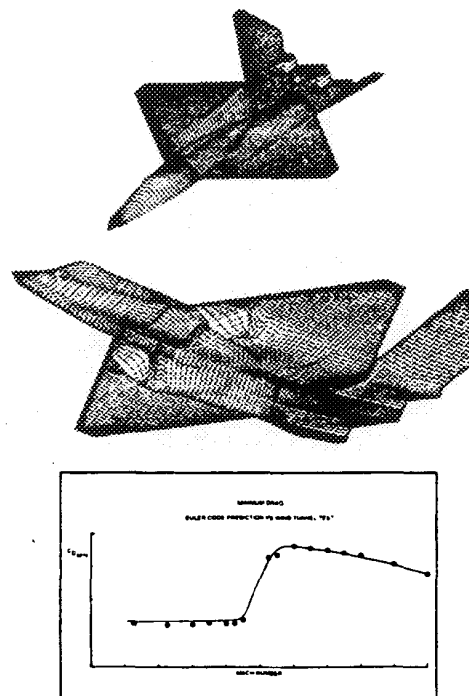


Figure 7: Comparison of Experimental and Computed Drag Rise Curve for the YF-23 (Supplied by R. J. Bush Jr.)

results of calculations using the AIRPLANE code developed by A. Jameson and T.J. Baker, to solve the Euler equations on an unstructured mesh. This provides the flexibility to treat arbitrarily complex configurations without the need to spend months developing an acceptable mesh. Figures 8 and 9 show calculations for supersonic transport configurations which were performed by Susan Cliff. The agreement with experimental data is quite good, and it has also been possible to predict the sonic boom signature [9].

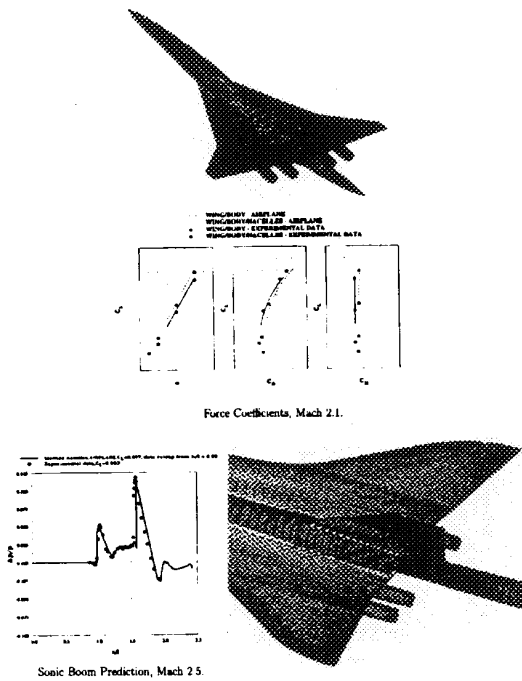


Figure 8: Comparison of Experimental and Calculated Results for a HSCT Configuration

3.2 Viscous Flow Discretizations

The results of the computations presented in the previous section prove that the Euler equations may provide a good approximation of the flow past aircraft. However viscous effects must be included for the correct prediction of performance. We have noted that the development and validation of turbulence models is one of the major hurdles toward the successful simulation of high Reynolds number flow. We also argued that the validation of turbulence models must rely on a direct comparison of numerical solutions with experiments. Thus, the accuracy of discretization of the viscous terms needs to be verified first. This Section reviews some of the algorithmic issues in discretization of the viscous terms. The following Sections present examples of verification and validation for viscous flows of progressively increasing complexity.

3.2.1 Discretization of the Viscous Terms

The discretization of the viscous terms of the Navier Stokes equations requires an approximation to the velocity derivatives $\frac{\partial u_i}{\partial x_j}$ in order to calculate the tensor σ_{ij} . Then the viscous terms may be included in the flux balance. In order to evaluate the derivatives one may apply the Gauss formula to a control

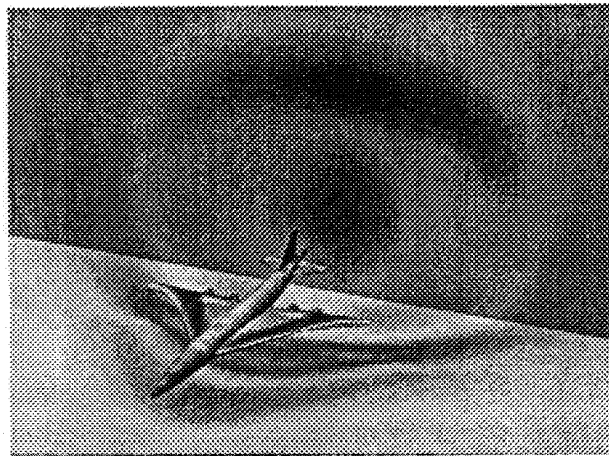


Figure 9: Pressure Contours and Sonic Boom on a Representative HSCT Configuration

volume V with the boundary S .

$$\int_V \frac{\partial u_i}{\partial x_j} dv = \int_S u_i n_j ds$$

where n_j is the outward normal. For a tetrahedral or hexahedral cell this gives

$$\overline{\frac{\partial u_i}{\partial x_j}} = \frac{1}{\text{vol}} \sum_{\text{faces}} \bar{u}_i n_j s \quad (1)$$

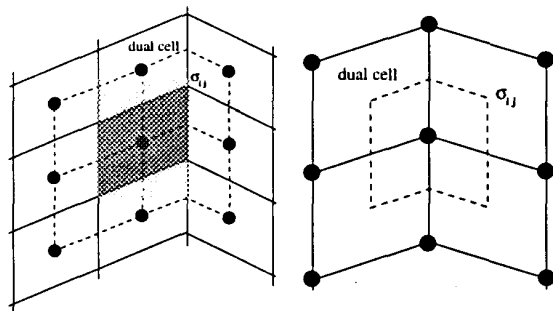
where \bar{u}_i is an estimate of the average of u_i over the face. If u varies linearly over a tetrahedral cell this is exact. Alternatively, assuming a local transformation to computational coordinates ξ_j , one may apply the chain rule

$$\frac{\partial u}{\partial x} = \left[\frac{\partial u}{\partial \xi} \right] \left[\frac{\partial \xi}{\partial x} \right] = \frac{\partial u}{\partial \xi} \left[\frac{\partial x}{\partial \xi} \right]^{-1} \quad (2)$$

Here the transformation derivatives $\frac{\partial x_i}{\partial \xi_j}$ can be evaluated by the same finite difference formulas as the velocity derivatives $\frac{\partial u_i}{\partial \xi_j}$. In this case $\frac{\partial u}{\partial \xi}$ is exact if u is a linearly varying function.

For a cell-centered discretization (figure 10a) $\frac{\partial u}{\partial \xi}$ is needed at each face. The simplest procedure is to evaluate $\frac{\partial u}{\partial \xi}$ in each cell, and to average $\frac{\partial u}{\partial \xi}$ between the two cells on either side of a face [21]. The resulting discretization does not have a compact stencil, and supports undamped oscillatory modes. In a one dimensional calculation, for example, $\frac{\partial^2 u}{\partial x^2}$ would be discretized as $\frac{u_{i+2} - 2u_i + u_{i-2}}{4\Delta x^2}$. In order to produce a compact stencil $\frac{\partial u}{\partial x}$ may be estimated from a control volume centered on each face, using formulas (1) or (2) [31]. This is computationally expensive because the number of faces is much larger than the number of cells. In a hexahedral mesh with a large number of vertices the number of faces approaches three times the number of cells.

This motivates the introduction of dual meshes for the evaluation of the velocity derivatives and the flux balance as sketched in figure 10. The figure shows



10a: Cell-centered scheme. σ_{ij} evaluated at vertices of the primary mesh
 10b: Cell-vertex scheme. σ_{ij} evaluated at cell centers of the primary mesh

Figure 10: Viscous discretizations for cell-centered and cell-vertex algorithms.

both cell-centered and cell-vertex schemes. The dual mesh connects cell centers of the primary mesh. If there is a kink in the primary mesh, the dual cells should be formed by assembling contiguous fractions of the neighboring primary cells. On smooth meshes comparable results are obtained by either of these formulations [27, 28, 26]. If the mesh has a kink the cell-vertex scheme has the advantage that the derivatives $\frac{\partial u_i}{\partial x_j}$ are calculated in the interior of a regular cell, with no loss of accuracy.

A desirable property is that a linearly varying velocity distribution, as in a Couette flow, should produce a constant stress and hence an exact stress balance. This property is not necessarily satisfied in general by finite difference or finite volume schemes on curvilinear meshes. The characterization k -exact has been proposed for schemes that are exact for polynomials of degree k . The cell-vertex finite volume scheme is linearly exact if the derivatives are evaluated by equation (2), since then $\frac{\partial u_i}{\partial x_j}$ is exactly evaluated as a constant, leading to constant viscous stresses σ_{ij} , and an exact viscous stress balance. This remains true when there is a kink in the mesh, because the summation of constant stresses over the faces of the kinked control volume sketched in figure 10 still yields a perfect balance. The use of equation (2) to evaluate $\frac{\partial u_i}{\partial x_j}$, however, requires the additional calculation or storage of the nine metric quantities $\frac{\partial u_i}{\partial x_j}$ in each cell, whereas equation (1) can be evaluated from the same face areas that are used for the flux balance.

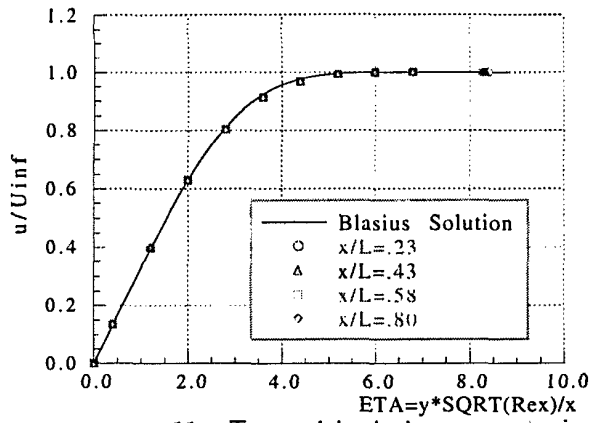
In practice it is important to reduce both the computational time and memory requirements in order to limit the computational cost. The examples below

are focussed on the verification and validation of the simplest possible cell-centered and vertex schemes, using the finite volume approach defined by equation (1) to evaluate the derivatives. In every case a major consideration is the need to use a mesh with small enough intervals in the boundary layer to make sure that the numerical diffusion introduced by the discretization is small in comparison with the true viscous terms.

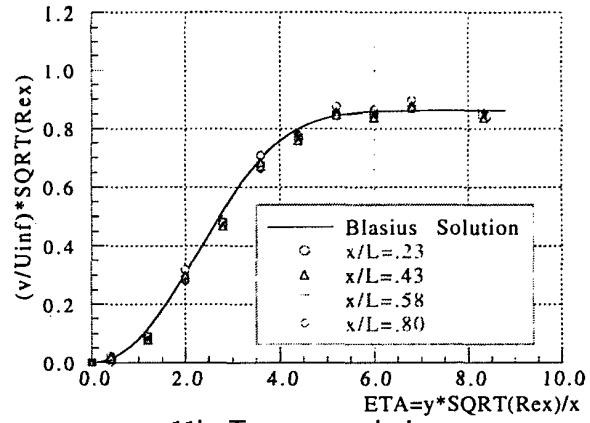
3.2.2 Flat-plate laminar boundary layer

A laminar boundary layer developing over a flat-plate at zero incidence is generally chosen as the first test case to validate schemes for the viscous flow problems. In our case the computational domain is a rectangle with the inflow boundary located two plate lengths upstream of the leading edge, and the downstream boundary located at the plate trailing edge. The upper boundary is located at a distance of four plate lengths. The mesh points are clustered in the streamwise direction near the leading edge, in order to provide adequate resolution of the flow near the stagnation point. The finest grid contains a total of 512 cells in the streamwise direction with 384 cells placed along the plate. Within the boundary layer, the grid is *equally spaced* in the boundary layer coordinate in the direction perpendicular to the plate. This ensures a constant level of resolution for all the boundary layer profiles. It also ensures that an identical resolution is achieved independently of the Reynolds number. Outside of the boundary layer the grid is exponentially stretched toward the far field. The finest grid contains a total of 128 cells in the direction normal to the plate, half of which are within the boundary layer. Three coarser grids containing respectively 8, 16, 32 cells within the boundary layer were obtained by elimination of alternate points, and they were used in the grid refinement study.

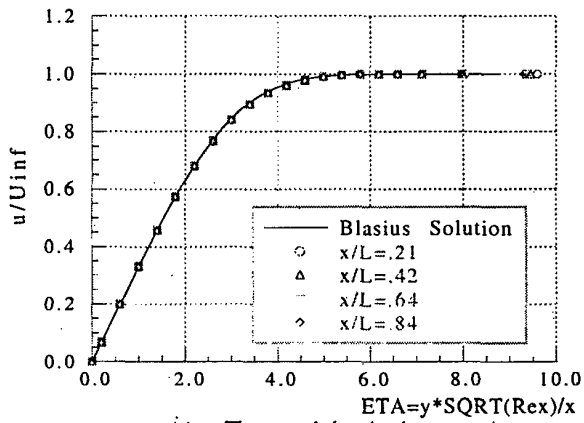
Previous studies have shown that 32 cells are generally sufficient to resolve the viscous layer [27]. Figure 11 shows the result of a grid refinement study on boundary layer velocity profiles, which was carried out to investigate the accuracy of the cell-centered H-CUSP scheme. The numerical diffusion introduced by this scheme approaches zero as the local velocity approaches zero, and this scheme is therefore particularly suitable for the treatment of viscous boundary layers. All the parameters of the numerical scheme are identical to those used for solving the Euler equations in the computation of the results presented in section 3.1. A low value of the incoming flow Mach number ($M_\infty = .15$), well within the incompressible regime, was chosen to make a comparison with a Blasius solution meaningful.



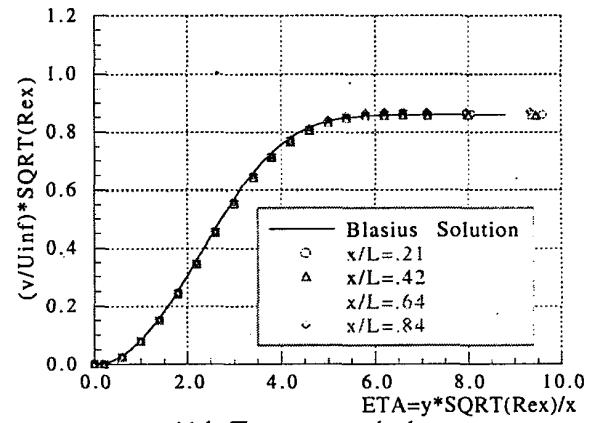
11a: Tangential velocity
8 cells in the layer



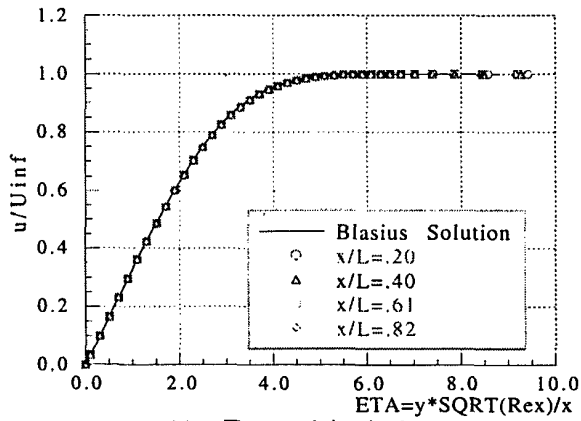
11b: Transverse velocity
8 cells in the layer



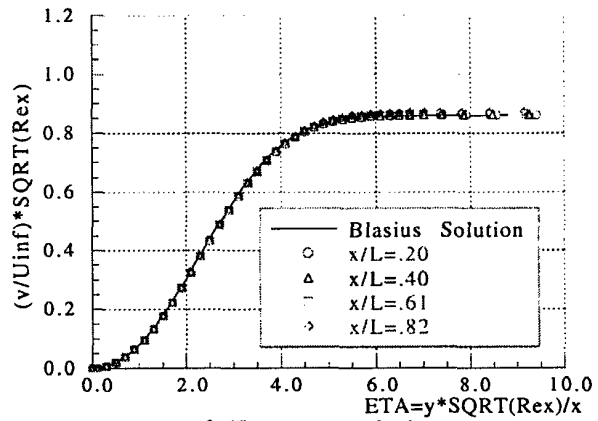
11c: Tangential velocity
16 cells in the layer



11d: Transverse velocity
16 cells in the layer



11e: Tangential velocity
32 cells in the layer



11f: Transverse velocity
32 cells in the layer

Figure 11: Boundary layer velocity profiles at $M = .15$ and $Re = 100,000$

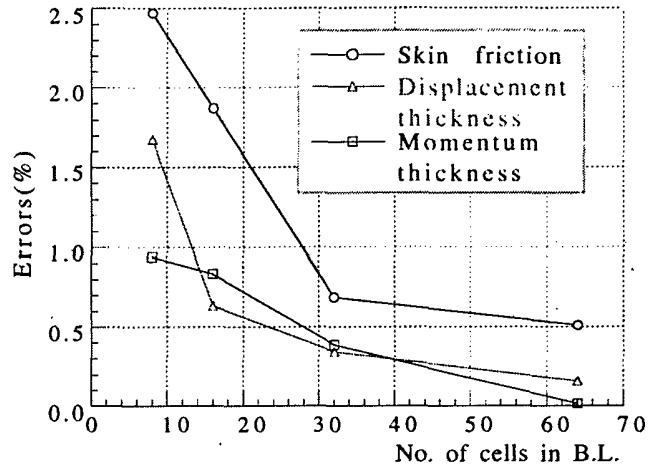


Figure 12: Comparison of computed results with the Blasius solution at $M = .15$ and $Re = 100,000$

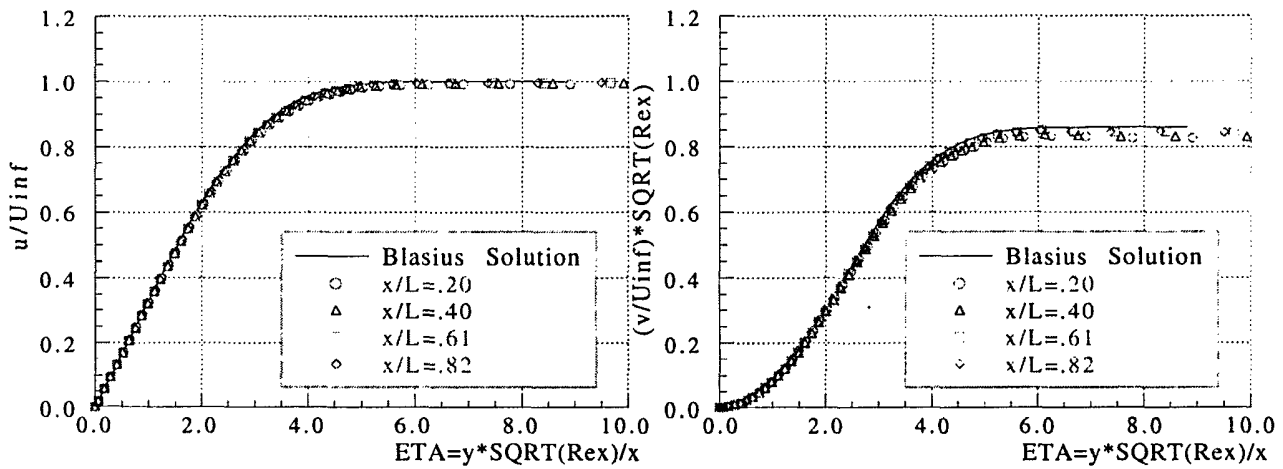


Figure 13: Boundary layer velocity profiles at $M = 2.0$ and $Re = 100,000$

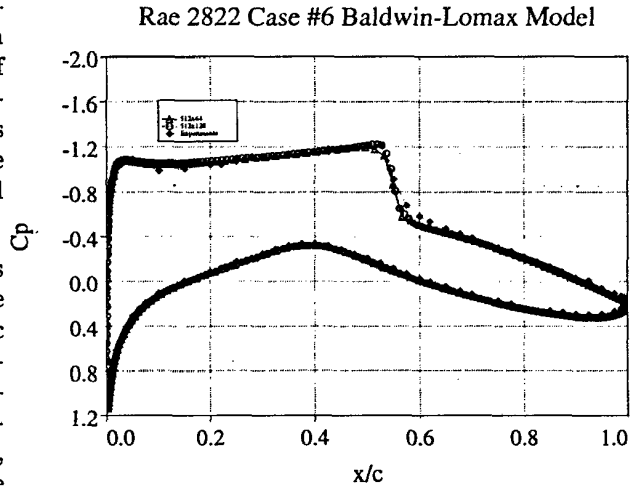
Also, this flow condition tests the numerical scheme toward its limit of applicability as $M_\infty \rightarrow 0$, and the flow becomes incompressible. The Reynolds number of the incoming flow is 100,000. The results at four streamwise locations are overplotted to verify the self similarity of the computed flow. It can be seen that both of the computed tangential and transverse components of the velocity follow the self similarity law, and give an excellent agreement with the Blasius solution even on the coarsest grid with 8 cells in the boundary layer. Figure 3.2.2 shows the errors of the computed skin friction, as well as the displacement and momentum thicknesses from the Blasius solution. While the errors decrease according to the grid refinement, the values themselves are very small even in the case of the coarsest grid.

The set of calculations presented in Figure 13 is aimed at investigating the behavior of the scheme as the Mach number increases into the supersonic regime. Results are presented for a Reynolds number of 100,000, on a grid with 32 cells in the boundary layer. The supersonic result is scaled by using the Illingworth - Stewartson transformation [35], and again compared with the Blasius solution. The result verifies the scheme in the supersonic regime.

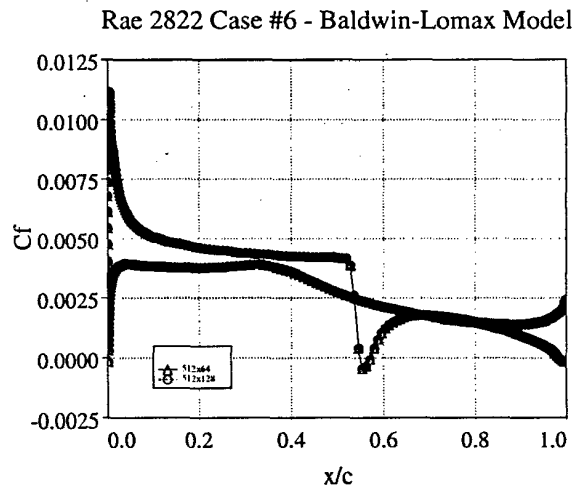
3.2.3 Two-dimensional turbulent flows

The first set of calculations in this section is designed to validate of the cell-centered H-CUSP scheme for a turbulent flow over a two dimensional airfoil. The RAE-2822 test Case 6 was selected [15]. Two meshes were used for the computations. The first consists of a total of 512×64 mesh cells with 385 points fitted on the airfoil, while in the second one the number of cells in the normal direction has been doubled to 128. The minimum distance from the airfoil surface of the first coordinate line is 2×10^{-5} chords which corresponds to a value of $y^+ < 5$ for the assigned Reynolds numbers, and the outer boundary was placed at a distance of 18 chords. Transition was fixed at the experimental location of the trip wire. A Baldwin and Lomax turbulence model [3] has been used for this grid refinement study because the flow field was expected to be attached, and the behaviour of the solution predicted by this model is reasonably well understood.

Figure 14 shows a comparison of the computed pressure coefficient along the airfoil for the two grid densities. The experimental results are also plotted as a reference. It can be seen that the computed pressure distribution is well converged on the 512×64 grid. The computed skin friction coefficient, normalized by the free stream dynamic pressure, is also plotted in figure 14, and shows that grid independent results are obtained on the 512×64 mesh.

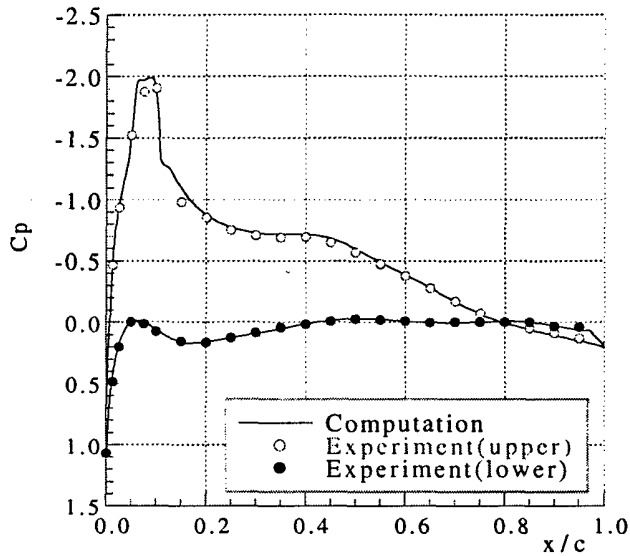


14a: Computed Pressure Distribution

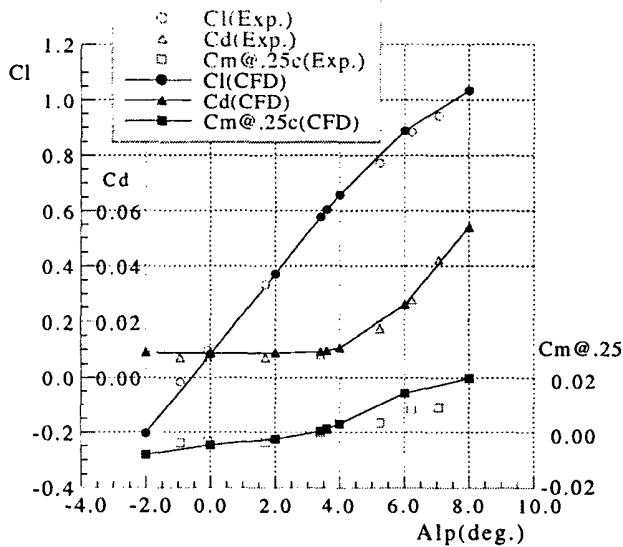


14b: Computed Skin Friction

Figure 14: Rae 2822 Case 6, $M = .731, \alpha = 2.51^\circ$, and $Re = 6,500,000$



15a: Pressure distribution
 $M = .59, \alpha = 3.41^\circ, Re = 7,500,000$



15b: $C_l, C_d,$ and $C_m(.25c)$
 $M = .59, Re = 7,500,000$

Figure 15: Comparison with Experimental data for RC(4)-10 Airfoil

Once the verification phase is concluded, the method is ready to be validated against independent experimental data. An example of validation presented next consists of a RC(4)-10 airfoil with a freestream Mach number of 0.59, and a Reynolds number of 7.5 million. The airfoil was designed for application to the inboard region of a helicopter main rotor blade [30]. This case was chosen to compare the prediction of the numerical scheme with independent experimental data. The turbulence model used here is again a simple algebraic Baldwin and Lomax. A C-type mesh consisting of a total of 512×64 mesh cells was used in the computations. The normal mesh spacing at the wall is 0.00002 chords, resulting in cells with aspect ratios of the order of 250:1 along the airfoil.

Figure 15 shows a comparison of the surface pressure distribution between the computed result and the experimental data at angle of attack of 3.41 degrees. The agreement is very good, including the shock location. The computed lift, drag, and pitching moment coefficients in terms of the angle of attack are shown in Figure 15 in comparison with experimental data. The agreement is again good except at the higher angle of attack. Here it is questionable whether the flow is truly steady. This calculation, therefore, contributes to the validation of the numerical approach for the simulation of attached viscous turbulent flows in the transonic regime.

3.2.4 Three-Dimensional Computations

The first set of computed results presented here is aimed at verifying the accuracy achieved by the cell-vertex finite volume scheme for vortex-flow applications. We conducted a numerical simulation of the flow over a cropped delta wing with a sharp leading edge. Both the geometry and the flow conditions corresponds to those tested by Hummel [6]

The relatively low Reynolds number (based on the root chord) of the experiments ($Re = 440,000$), allowed the calculation of the viscous flow to be successfully computed by using the pure Navier-Stokes formulation. By avoiding any uncertainty attributable to turbulence modeling, it provides us with an ideal test-case for the validation of our method for vortex-dominated flows. A $161 \times 49 \times 49$ C-H grid was employed [28] A comparison of the results for two cross-sections of the wing are reported here. Figure 16 shows a comparison of the pressure coefficient on three cross-sectional cuts of the wing computed by modeling the flow using the Navier-Stokes equations and the Euler equations. It can be seen that the two mathematical models are in good agreement in the inboard section of the wing, whereas they differ substantially in the outboard re-

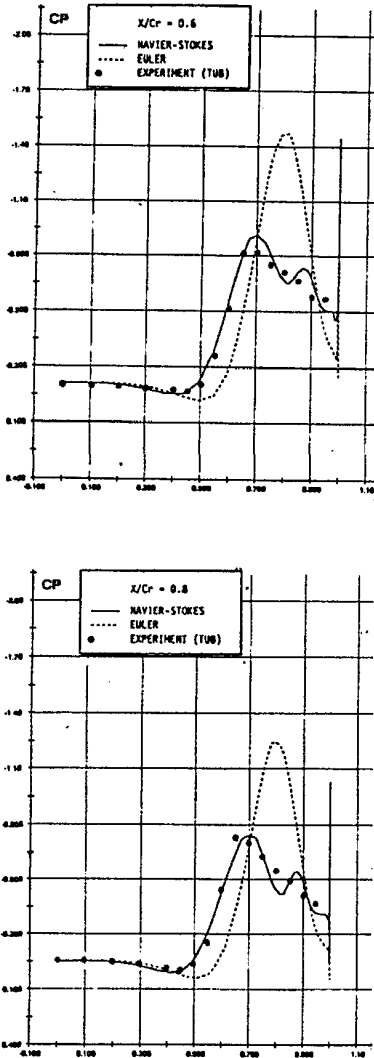


Figure 16: Comparison with Experimental data Laminar Flow over A Delta Wing

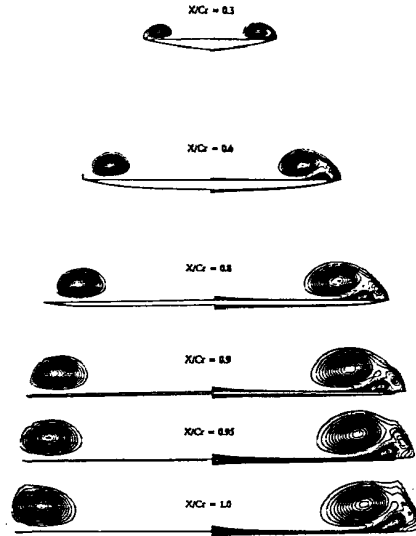


Figure 17: Comparison of Euler (left) and Laminar Flow over A Delta Wing

gion. Moreover, the position of the primary vortex, for both the Euler and the Navier-Stokes solutions, compare reasonably well with experiments, and the results of the viscous simulation are also in good agreement with the measurements in the region of the secondary vortex. The visualization of the vortical flow by the computed total pressure contours of Figure 17 confirms the expectation that the computed evolution of the primary vortex is not strongly affected by the effects of viscosity. We can also verify that the viscous effects are responsible for the generation of a secondary vortex, which is absent in the inviscid calculation, and that alters the load distribution on the wing.

The next set of computations corresponds to the turbulent flow simulation on the ONERA-M6 wing at $M = 0.84$, $Re = 11.7$ million and $\alpha = 3.06^\circ$. The calculation was performed on a $193 \times 65 \times 49$ C-H grid using the vertex based formulation with the H-CUSP scheme. A Johnson and King turbulence model was adopted. Figure 18 shows the comparison of measured and computed pressure coefficients at four spanwise stations.

The next set of computations corresponds to the turbulent flow simulation on a cropped delta wing wing at $M = 0.85$, $Re = 9$ million and $\alpha = 10^\circ$ [13]. The calculations were performed on a $193 \times 65 \times 96$ C-H grid was using the vertex based formulation. Again the H-CUSP scheme was adopted in conjunction with a Johnson and King turbulence. Figure 19 shows a comparison of measured and computed pressure coefficients at three spanwise stations. It can be seen that the agreement is rather good, and the footprint of the primary vortex is at the right

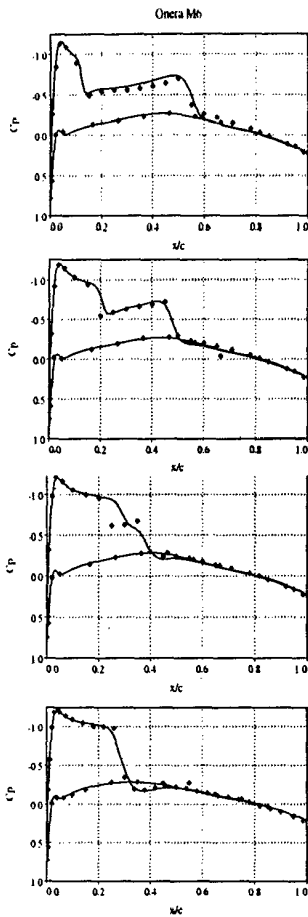


Figure 18: Comparison of Experimental and Computed Pressure Coefficients for the ONERA-M6 Wing. Spanwise Cuts at .44, .65, .80, .90 (Top to Bottom). $M = .84, Re = 11.7\text{million}, \alpha = 3.06^\circ$.

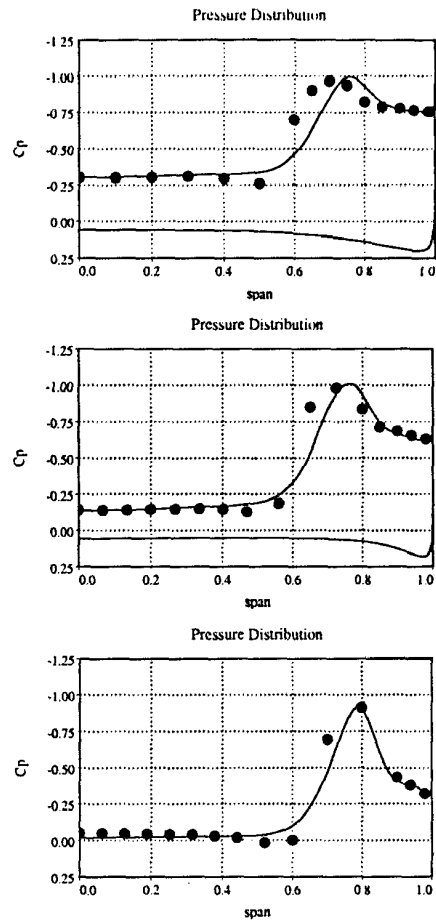


Figure 19: Comparison of Experimental and Computed Pressure Coefficients for a 65 deg Cropped Delta Wing. Chordwise Cuts at .6, .80, .967 (Top to Bottom). $M = .85, Re = 9\text{million}, \alpha = 10.0^\circ$.

location, and the experimental pressure plateau in the outboard region is recovered. The vortical flow is visualized in Figure 20 by using iso-contours of total pressure. It should be noted that the vortical structures are captured very sharply by the H-CUSP scheme.

3.3 Time-Resolved Inviscid Flow Simulations

The following two sections, present examples of the verification and validation of fully implicit time-stepping schemes which have been used to allow the time step to be determined purely by accuracy requirements in the simulation of both inviscid and viscous flows. Backward difference schemes of arbitrarily high order can be used to approximate the time derivatives. The second order scheme is A-stable, while the third and fourth order schemes are stiffly stable. The implicit equations for a single time step are then solved by an inner time stepping scheme

with variable local time steps and multigrid acceleration [18]. This method has also been extended for incompressible flows in collaboration with A. Belov. For this purpose, artificial compressibility is used in the inner time stepping scheme [5].

3.3.1 Oscillating Airfoil in Compressible Flow

A series of computation were carried out by J. Alonso [2] for verification and validation of the inviscid implicit scheme originally proposed by Jameson [18]. A NACA 64A010 airfoil section was used at a free stream Mach number $M_\infty = 0.796$, and 36 equal real time steps per period of forced oscillation were taken. The airfoil was forced in pitch about the quarter chord at a reduced frequency of 0.202. Experimental results are available for this test case [11]. As we can see in Figure 21, the results computed with a second order backward formula, are in good agreement with the experiment, validating

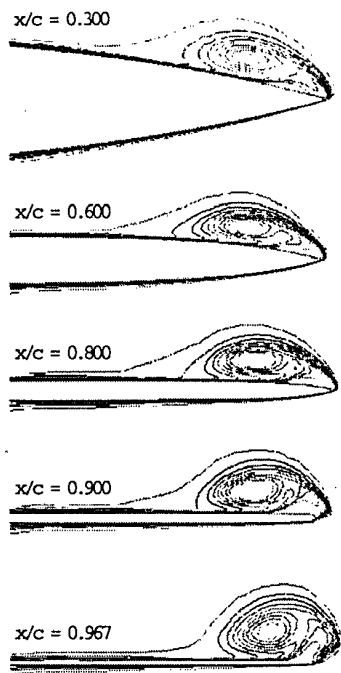


Figure 20: Iso-countours of Computed Total Pressure Coefficient for a 65 deg Cropped Delta Wing. Chordwise Cuts at .3,.6,.80,.9,.967 (Top to Bottom). $M = .85, Re = 9\text{million}, \alpha = 10.0^\circ$.

this efficient algorithm for inviscid simulation. Further verification, has been carried out but using the third- and fourth- order accurate discretizations of the time derivative operator. The third-order accurate discretization yields a considerable improvement over the baseline discretization. As we can see in Figure 22 the computations with the third-order accurate discretization using 12 and 8 steps per period are barely distinguishable from the second order accurate results using 72 steps per period. The third-order accurate algorithm has a storage penalty since one extra level of computations needs to be stored. For Euler flows, this penalty is greatly outweighed by the savings in processor time that result from a maximum CFL number on the order of 12,000 in the smallest cells of the domain.

3.3.2 Oscillating Circular Cylinder in Incompressible Flow

The flow over a sinusoidally oscillating circular cylinder represents a good test for verification of numerical methods for inviscid incompressible flow. An analytic solution is known, and it provides a severe test for the computational algorithm since no physical dissipation is present. The diameter of a cylinder

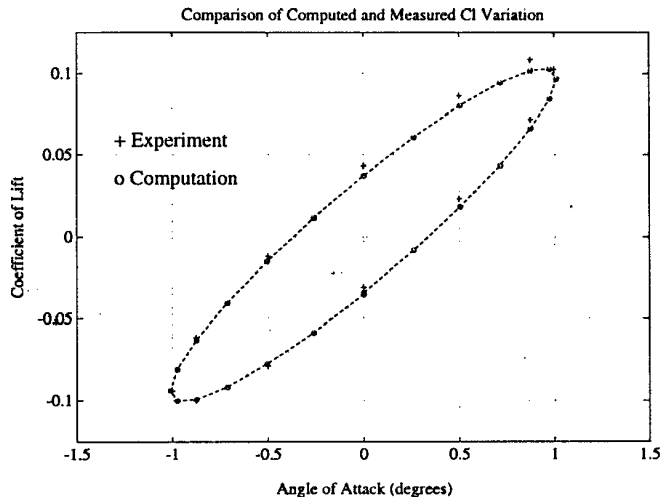


Figure 21: Comparison of Calculated and Experimental Results [25].

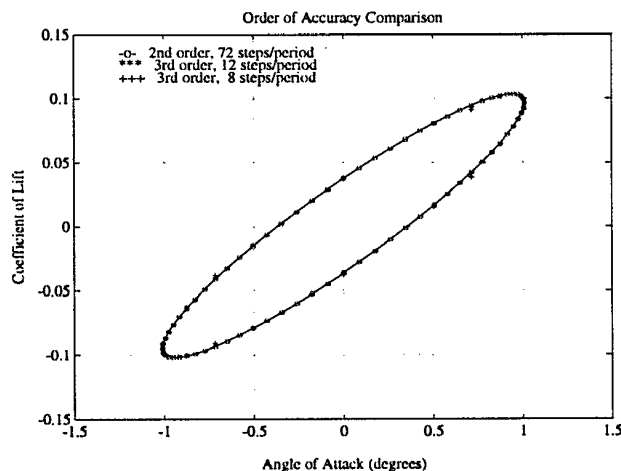


Figure 22: Comparison between Second- and Third-Order Accurate Calculations.

and a period of forced oscillations are chosen to be the length and the time scales of the problem, so that the nondimensional frequency $f = 1$ results. The coordinate of the center of a cylinder is set to

$$x_{cyl}(t) = a \cdot \sin(\omega t - \varphi),$$

where the motion amplitude a is equal to 0.1 and the initial phase φ is 90° . The fluid velocity and the static pressure at infinity P_∞ are assumed to be zero. The exact solution for the incompressible inviscid flow over a moving cylinder can be found in [25]. The velocity field and the surface pressure distribution reduce in this case to

$$\begin{aligned} u(\theta, t, r) &= \frac{0.25}{r^2} \cdot u_{cyl}(t) \cdot \cos 2\theta, \\ v(\theta, t, r) &= \frac{-0.25}{r^2} \cdot u_{cyl}(t) \cdot \sin 2\theta, \end{aligned} \quad (3)$$

$$P_s(\theta, t) = P_\infty + u_{cyl}^2(t) \cdot (2 \cos^2 \theta - 1.5) + \frac{du_{cyl}(t)}{2 dt} \cdot \cos \theta;$$

where r is the distance to the center of a cylinder and θ is measured clockwise from the direction of the x -axis. The third term in the pressure equation produces a nonzero net contribution to the dynamic drag force acting on a cylinder. The resulting drag coefficient due to the apparent mass effect is

$$C_{d_{cyl}}(t) = \frac{a\omega^2\pi}{2} \cdot \sin(\omega t - \varphi). \quad (4)$$

In order to verify the implicit scheme, a grid refinement study was carried out using three O-meshes rigidly attached to the cylinder consisting of 65×33 , 129×65 and 257×129 grid points respectively [5]. The cylinder is initially at rest with $x_{cyl}(0) = -a$. The time step is $\Delta t = 0.025$ and the far field boundary is placed 16 diameters away from the center of the cylinder. On each grid, the maximum modified residual in the divergence equation is reduced below 10^{-4} at each time step using approximately 50 multigrid W-cycles. The evolution of the drag coefficient computed on the 65×33 grid is compared in Figure 23 with the exact solution (Equation 4), which is shown using a solid line. The calculation on the coarsest grid is found to overpredict the maximum drag amplitude by approximately 1.7%, while the results for the two finer grids coincide with the solid line.

The order of convergence in the grid refinement study can be estimated by the logarithm of the ratio of the computed drag amplitudes

$$\log_2 \left(\frac{\max(Cd_{65 \times 33}) - \max(Cd_{129 \times 65})}{\max(Cd_{129 \times 65}) - \max(Cd_{257 \times 129})} \right) = 1.84,$$

which is close to 2. This is indeed consistent with the second order accuracy of the spatial discretization which was used. The pressure and velocity distributions on the surface of the cylinder, given by

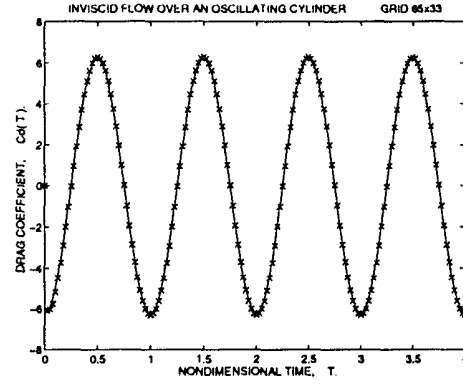


Figure 23: Drag Coefficient for an Oscillating Cylinder.

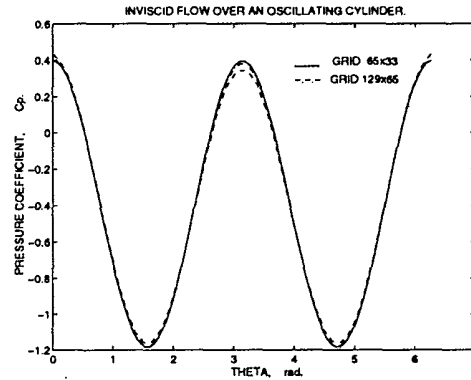


Figure 24: Surface Pressure Coefficient for an Oscillating Cylinder, $t = 4.25$.

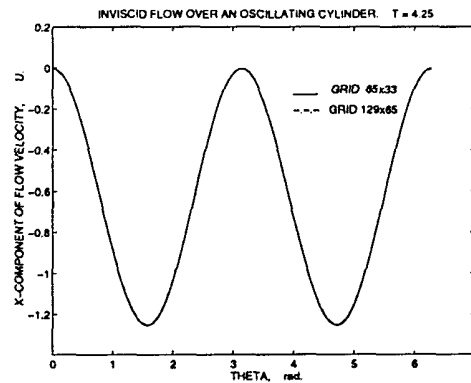


Figure 25: Surface x-Component of the Velocity for an Oscillating Cylinder, $t = 4.25$.

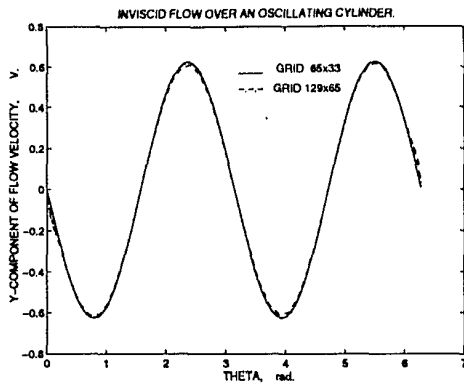


Figure 26: Surface y-Component of the Velocity for an Oscillating Cylinder, $t = 4.25$.

Equations 3, are plot in Figures 24, 25 and 26. The comparison between the computed results and the analytical solution is excellent. This validates the basic numerical approach for inviscid incompressible flow.

3.4 Time-Resolved Viscous Flow Simulations

3.4.1 Pitching NACA 64A010 Airfoil

In a previous Section, the inviscid flow over this airfoil has been calculated, and the unsteady C_l vs. α curve was found to agree quite well with the experiment. The experimental results lie on a periodic curve in the shape of an oval, which is slightly broader than the inviscid calculations. In Figure 27 we can see that the inclusion of viscous effects tilts the inviscid oval in the direction of the experimental results. The very slight difference still existing can be due to inaccuracies in the turbulence model. For attached flows, we can conclude that inviscid solutions are the best compromise for the prediction of lift related properties.

However, if in addition one wants to obtain drag and pitching moment information, the only option is to use the full Navier-Stokes equations with a suitable turbulence model. Figure 28 shows the motion of the shocks in the upper and lower surfaces of the airfoil for a little more than half a pitching cycle. The snapshots are arranged by rows. As the airfoil pitches up, the shock in the upper surface moves aft at the same time as it becomes stronger. The shock in the lower surface moves forward, weakens, and disappears. As the airfoil pitches down, the opposite begins to happen, with a small phase lag. By virtue of the use of the H-CUSP, shocks can be resolved very crisply, with the additional advantage that the actual viscosity in the flow field is contaminated to a much lesser degree. Finally, Figure 29 shows the coeffi-

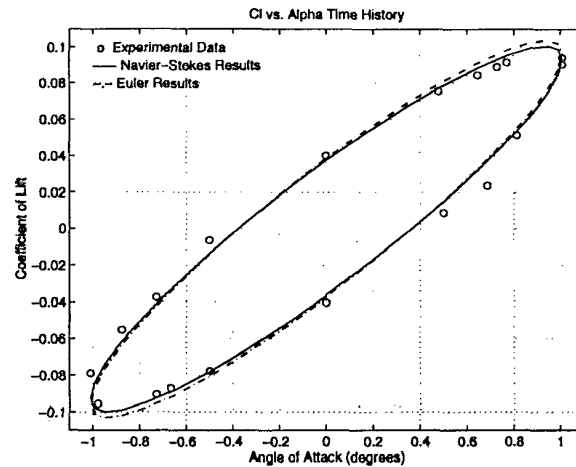


Figure 27: Coefficient of Lift Time History.

cient of pressure along a coordinate line that circles the airfoil right outside of the boundary layer. One can clearly see that these the results, which were obtained with the H-CUSP scheme, are superior to those that could be obtained with a scalar dissipation model which spreads the shock over 4 or 5 cells instead of 1 or 2.

3.4.2 Incompressible Vortex Shedding

For time-accurate calculations, a verification of the order of accuracy of the time-marching scheme is also necessary in addition to the standard verification of the accuracy in space. Thus it is advisable to compute a given benchmark problem, and compare the results computed with a sequence of progressively smaller time steps. The benchmark problem selected here is the parallel vortex shedding behind a half-cylinder corresponding to a Reynolds number 250 based on the diameter. This is a very challenging and interesting problem which has been computed by other authors with high order spectral elements method [17]. When the integration is carried out for a long time, this flow exhibits a secondary instability leading to vortex pairing. Figure 30 shows the results a time resolution study performed with a second order accurate, A-stable backward difference scheme on a 192×384 O-mesh, with the far field located 45 diameters from the body. For this case, the shedding frequency is approximately .2. Thus, one full shedding cycle takes approximately 5 time units to complete. It is noted that the results obtained with $\delta t = 5/48$ - corresponding to 48 time steps per shedding cycle - almost overplot those obtained with a $\delta t = 5/96$ indicating that convergence of the time approximation has been reached. When a third order stiffly stable scheme is employed, the results for a time resolution study pre-

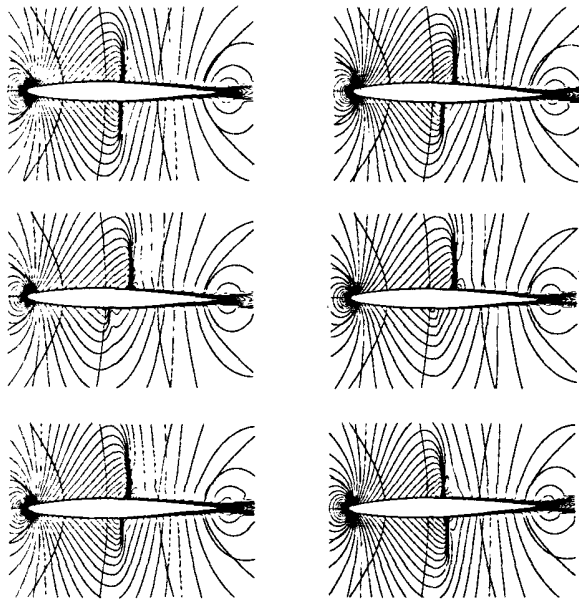


Figure 28: Mach Number Contours. Pitching Airfoil Case. $Re = 1.0 \times 10^6$, $M_\infty = 0.796$, $K_c = 0.202$.

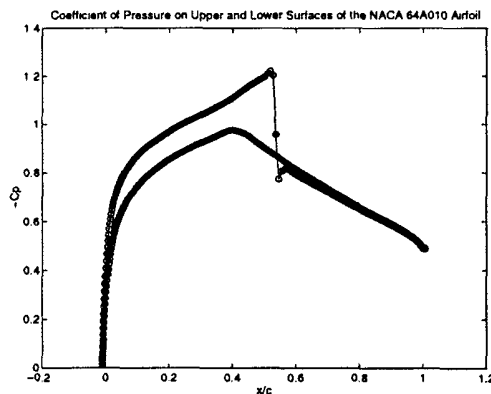


Figure 29: Coefficient of Pressure on a Grid Line at Edge of the Boundary Layer.

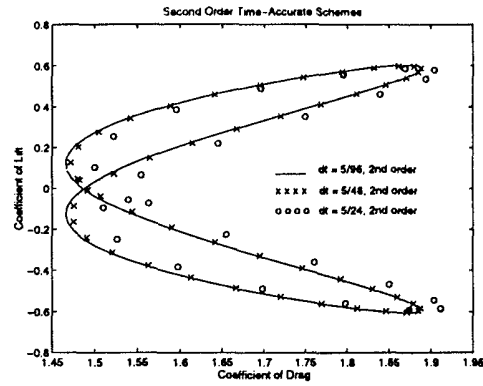


Figure 30: Drag Polar for a Half Cylinder Computed with a Second Order Accurate Scheme.

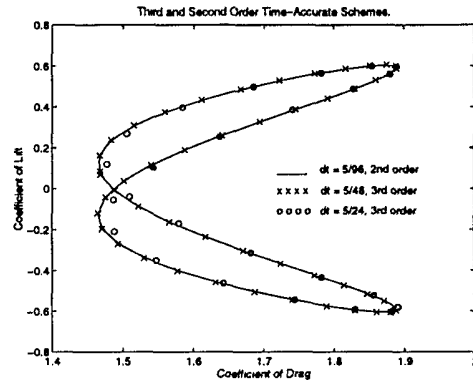


Figure 31: Drag Polar for a Half Cylinder Computed with a Third Order Accurate Scheme.

sented in figure 31 reveals that 48 time steps of the third order scheme are sufficient to resolve one shedding cycle to the same accuracy as the most refined calculations with the second order scheme.

Since in our implicit method the computational costs associated with increased time resolution reflects almost exclusively on memory, and not CPU, the net result of the time refinement study indicates a favorable trade off for the third order accurate scheme, which was then selected to carry out the final calculation of as many as 5000 shedding cycles necessary to observe the onset of the vortex pairing and gather mean flow quantities. The results of that calculation, which are not reported here for the sake of brevity, were found in excellent agreement with the one obtained by using higher order spectral methods. Thus, a study of time accuracy, and a favorable comparison with the results computed by other authors with higher order methods, provide a solid verification of the overall method. The final validation steady is described next.

The unsteady laminar vortex shedding from a circular cylinder for $Re \leq 300$, based on the cylinder diameter and a free stream velocity, was selected a

validation problem. This is a classical flow for which excellent experimental data at low Reynolds number are available. This shows that there is a sudden transition from two dimensional parallel shedding to three dimensional shedding. Recent experimental studies of the wake of circular cylinders [44] showed that a parallel shedding can be observed in the range of $49 < Re < 180$, provided that special care is taken to control the end effects. Above $Re = 180$, three-dimensional shedding modes are observed, while for Reynolds numbers below 49 the wake is stationary.

For Reynolds number less than 150 the flow is essentially two dimensional. This allows the initial validation of the method to be carried out using a two-dimensional model. A 257×257 O-mesh with a normal spacing of the grid next to the surface of 0.0003 diameters was used in the calculations. A relatively fine resolution of approximately 0.1 diameter is maintained in the radial direction up to the far field boundary. The far field boundary is placed at a distance of 16 diameters from the center of the cylinder.

The converged Strouhal frequency for $Re = 150$ was found to be equal $St = 0.182$, while the values of the aerodynamic coefficients, corresponding to a limiting cycle, are: $Cl = 0.000 \pm 0.486$ and $Cd = 1.168 \pm 0.025$. Once the asymmetric shedding developed, 15 multigrid W-cycles using seven grid levels were sufficient to enforce the divergence free constraint in each cell better than 10^{-5} .

In order to assess the effects of the spatial discretization, the two auxiliary calculations with the $Re = 150$ are performed on two successively coarser grids with, respectively, 129×129 , and 65×65 grid points. The coarser grids are constructed by eliminating the alternate points from the finest 256×256 grid, resulting in a somewhat lower resolution in the boundary layer. The order of convergence can be estimated using the ratios of the amplitudes of the oscillations of the aerodynamic coefficients as well as the Strouhal numbers computed on the three grids

$$\log_2 \left(\frac{St_{65 \times 65} - St_{129 \times 129}}{St_{129 \times 129} - St_{257 \times 257}} \right) = 2.27,$$

$$\log_2 \left(\frac{\max(Cl_{65 \times 65}) - \max(Cl_{129 \times 129})}{\max(Cl_{129 \times 129}) - \max(Cl_{257 \times 257})} \right) = 1.83,$$

$$\log_2 \left(\frac{\max(Cd_{65 \times 65}) - \max(Cd_{129 \times 129})}{\max(Cd_{129 \times 129}) - \max(Cd_{257 \times 257})} \right) = 2.01,$$

which are indeed close to 2. This is consistent with the second order accuracy of the spatial discretization and also in agreement with the value obtained for the inviscid calculations above.

The laminar wake flow with $Re = 200$ has been considered by many authors as a test case, and some

Reference	Cl	Cd	St
Present	± 0.64	1.19 ± 0.041	.196
Rogers, Kwak	± 0.65	1.23 ± 0.05	.185
Miyake et al.	± 0.67	1.34 ± 0.043	.196
Lecointe et al.	± 0.5	1.58 ± 0.0035	.194
Lin et al.		1.17	
Henderson			.197
Kovaznay (exp.)			.19
Roshko (exp.)			.19
Roshko (fit.)			.190
Williamson (fit.)			.197

Table 3: Flow over a circular cylinder at Reynolds number 200: coefficients of lift and drag and Strouhal number.

of the relevant data, quoted from from the literature, are presented in Table 3. However, according to [44], three-dimensional vortex shedding occurs at this Reynolds number. Also, the results in [17] suggest that the continuation of the “universal curve” corresponding to the parallel shedding (see the analysis below) and represented by the last entry in Table 3, might provide a better basis for validation of two-dimensional computations, then the actual experimental data for this particular Reynolds number. Taking into account those considerations, and especially in view of the wide scattering of the data in Table 3, it appears that a lower Reynolds number flow ($Re = 150$ for example) would provide a more meaningful validation of the two-dimensional numerical computations.

A continuous relation $St(Re)$ of the form

$$St(Re) = \frac{A}{Re} + B + C \cdot Re, \quad (5)$$

where A, B and C are constants, was proposed by Williamson [43] to describe the parallel vortex shedding believed to be accurate within 1%. The computed $St(Re)$ data for the set of calculations in the range of $Re \leq 200$ are compared with the experimental curves and other computations [33, 44, 17] in Figure 32. The curve fitting coefficients, corresponding to Equation 5, which were used for the comparison, are summarized in Table 4.

The experimental data of Williamson [44] are shown in Figure 32 for the range $49 < Re < 180$ by a solid line with the ticks indicating an estimated accuracy of $\pm 1\%$. The present data are found to be in excellent –better than 1%– agreement with the “universal curve” in this range of Reynolds numbers [43]. Our data are also in good agreement with the experimental curve obtained by Roshko [33] and the unstructured spectral element computations by Henderson [17].

The computed variation of the base pressure coef-

Source	Quantity	A	B	C · 10 ⁴
[43]	St	-3.3265	.1816	1.600
[33]	St	-4.50	.212	—
[17]	St	-3.3658	.1831	1.627
[44]	Cpb	-14.3500	.6950	16.920
[17]	Cpb	-10.1090	.6380	20.570

Table 4: The “universal curve” coefficients for the mean flow quantities in the wake of a circular cylinder.

cient with Reynolds number $Cpb(Re)$ is shown in Figure 33. Our data exhibit the same trend as other computational and experimental results [17, 33], yet they differ from the latter by 2 or 3%. This is within experimental errors. Below $Re < 49$, the wake is stationary. A decaying response is observed in the calculations, confirming that the present method captures correct the asymptotic behavior of wake flows for the range of Reynolds numbers considered.

In order to simulate the transition to three dimensional shedding, three-dimensional computations were performed on a $96 \times 64 \times 32$ O-H-mesh for a cylinder with an aspect ratio $L/D = 6.4$. Periodic boundary conditions were imposed along the span. An initial disturbance was introduced in the flow to expedite the onset of the shedding. The results for $Re = 150$ exhibits a decaying response to the initial disturbance and reach, asymptotically, a two-dimensional shedding, which is in agreement with the experimental predictions. At $Re = 225$ the flow is unstable to the same disturbance: initially the flow develops essentially two-dimensional shedding, and then, the $d(Cpb)$ and the maximum spanwise velocity component gradually increases by two orders in magnitude until a fully three dimensional shedding is established. The time-averaged flow quantities corresponding to the initial parallel shedding regime agree reasonably well with those computed by the two-dimensional solver, as given in Table 4, despite the difference in spatial resolution of the two meshes. An identical behaviour has been verified at $Re = 250$. Thus, at least for the two Reynolds number computed, our model reproduces the expected transition from an initial parallel shedding to a fully three-dimensional regime, and the good agreement of both the computed Strouhal frequency and base pressure with the experimental data reinforces the validity of our numerical approach.

4. CONCLUSION

Our main conclusion is that validation of computational methods is not simply a matter of comparing numerical results with experimental data. One must begin by establishing that the mathematical model

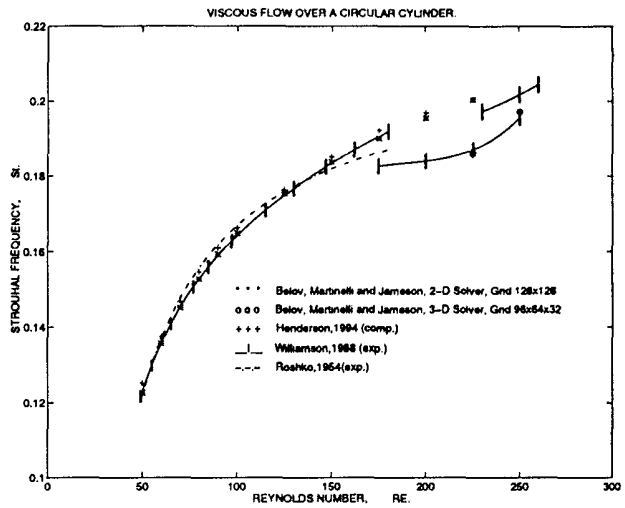


Figure 32: Strouhal Frequency as Function of Reynolds Number.

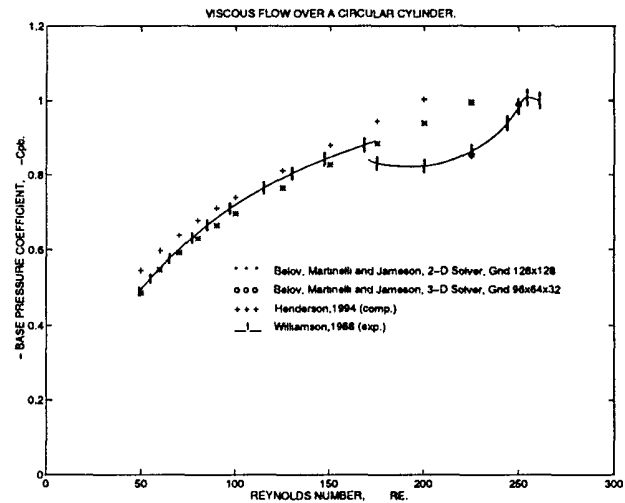


Figure 33: Base Pressure Coefficient as Function of Reynolds Number.

is logically consistent, and that it is approximated by a correct numerical method, which is in turn implemented in a correct computer program. Only then can a comparison with experimental data be used to determine whether the mathematical model incorporates enough of the true physics to make useful predictions for the purpose in hand. If it is first established, for example, that a numerical method accurately solves the incompressible potential flow equations, then comparisons with experimental data can be used to determine whether this model adequately represents any real flows. Separated viscous flows clearly do not satisfy the assumptions used in the derivation of the potential flow equation. This the failure of the method to predict these flows would be perfectly consistent with the assumptions embedded in the method, and would not necessarily invalidate the use of the method to predict flows for which the assumptions are reasonably closed to being satisfied. In fact, potential flow models have been successfully used to predict a wide variety of attached flows at low Mach numbers.

With this understanding it is apparent that each step in the process of developing the final complete software needs to be independently verified and validated in every feasible way. First the assumptions of the formulation of the mathematical model need to be clearly defined and understood, and the logical consistency of the model needs to be verified. This includes the formulation of proper boundary conditions, and ideally proof that a solution exists and is both unique and well posed, depending continuously on the data. Next, it is necessary to derive a correct numerical approximation, and to verify both its consistency with the mathematical model, and its accuracy. Mesh refinement studies provide a primary tool for this purpose.

Then, one must try to establish that the implementation of the method in a computer program is correct. In the case of complex software this is extremely difficult. It may be very hard to detect an error, say by a factor of two, in some parameter that only has a small influence on the results. In the authors' experience it pays to divide the complete program into relatively small submodules. Then one or more alternate implementations of the submodules should be independently coded, and it should be verified that each alternate implementation can be substituted in the complete software while producing the same final results within round-off errors. It is also essential to conduct systematic testing of the software for every situation in which it might be used by varying the input parameters in all possible combinations. Finally, the confidence level in the correctness of computer programs can be increased by comparisons with other computer programs which are intended to represent the same model, provided

that the results agree.

Once it is established by logical analysis and testing that the computational method does provide a sufficiently accurate solution of the intended mathematical model, one can proceed to assess the validity of the assumptions of the model by comparisons with experimental data. Here it will often be the case that the model is only expected to be valid in a certain range (say of Reynolds and Mach numbers), and the validation will be used to determine the range of applicability of the software. This process can only be effectively carried out if the accuracy of the numerical method has first been independently verified. For example, in testing the predictions of a proposed turbulence model it is essential that one first establishes mesh independence of the numerical solution. A fine enough mesh with a good enough quality must be used to ensure that there are not significant variations in the solution when either the number or the placement of the mesh points is varied. Otherwise it is impossible to distinguish modelling errors from numerical errors. Thus we see software validation as a complex multifaceted process in which every component step in the production of the final complete software needs to be separately verified and validated.

4.1 ACKNOWLEDGEMENT

Our research has benefited greatly from the support of ARPA under Grant Number N00014-92-J-1796, ONR under Grant Number N00014-93-I-0079, AFOSR under Grant Number AFOSR-F49620-95-1-0259, and USRA through RIACS at the NASA Ames Research Center. The support provided by the IBM-CRA grant is also gratefully acknowledged by the authors.

REFERENCES

- [1] R. Abid, C.G. Speziale, and S. Thangam. Application of a new $k-\tau$ model to near wall turbulent flows. AIAA Paper 91-0614, AIAA 29th Aerospace Sciences Meeting, Reno, NV, January 1991.
- [2] J. J. Alonso and A. Jameson. Fully-implicit time-marching aeroelastic solutions. *AIAA paper 94-0056*, AIAA 32nd Aerospace Sciences Meeting, Reno, Nevada, January 1994.
- [3] B. Baldwin and H. Lomax. Thin layer approximation and algebraic model for separated turbulent flow. AIAA Paper 78-257, 1978.
- [4] B.S. Baldwin and T.J. Barth. A one-equation turbulence transport model for high Reynolds

- number wall-bounded flows. AIAA Paper 91-0610, AIAA 29th Aerospace Sciences Meeting, Reno, NV, January 1991.
- [5] A. Belov, L. Martinelli, and A. Jameson. A new implicit algorithm with multigrid for unsteady incompressible flow calculations. *AIAA paper 95-0049*, AIAA 33rd Aerospace Sciences Meeting, Reno, Nevada, January 1995.
- [6] A. Bergmann and D. Hummel. Pressure distributions on the flat surface wing wil. *Private Communication*, TU Braunschweig, 1990.
- [7] R.J. Busch, Jr. Computational fluid dynamics in the design of the Northrop/McDonnell Douglas YF-23 ATF prototype. *AIAA paper 91-1627*, AIAA 21st Fluid Dynamics, Plasmadynamics & Lasers Conference, Honolulu, Hawaii, 1991.
- [8] T. Cebeci and A.M.O. Smith. *Analysis of Turbulent Boundary Layers*. Academic Press, 1974.
- [9] S.E. Cliff and S.D. Thomas. Euler/experimental correlations of sonic boom pressure signatures. AIAA Paper 91-3276, AIAA 9th Applied Aerodynamics Conference, Baltimore, September 1991.
- [10] T.J. Coakley. Numerical simulation of viscous transonic airfoil flows. AIAA Paper 87-0416, AIAA 25th Aerospace Sciences Meeting, Reno, January 1987.
- [11] S.S. Davis. Naca 64 a010 (nasa ames model) oscillatory pitching. Agard report no. 702, 1982.
- [12] D. Degani and L. Schiff. Computation of turbulent supersonic flows around pointed bodies having crossflow separation. *J. Comp. Phys.*, 66:173-196, 1986.
- [13] A. Elsenaar and H.W.M. Hoeijmakers. An experimental study of the flow over a sharp leading edge cropped delta wing at subsonic, transonic and supersonic speed. NLR TP-91117L, 1991.
- [14] G.H. Golub and J.M. Ortega. *Scientific Computing and Differential Equations*. Academic Press, San Diego, 1992.
- [15] Cook P. H., Mc Donald M. A., , and Firmin M. C. P. Aerofoil rae 2822 pressure distributions , boundary layer and wake measurements. AGARD Advisory Report 138, AGARD, 1979.
- [16] M.H. Ha. The impact of turbulence modelling on the numerical prediction of flows. In M. Napolitano and F. Solbetta, editors, *Proc. of the 13th International Conference on Numerical Methods in Fluid Dynamics*, pages 27-46, Rome, Italy, July 1992. Springer Verlag, 1993.
- [17] R.D. Henderson. Unstructured spectral element methods: Parallel algorithms and simulations. *Princeton University Thesis*, June 1994.
- [18] A. Jameson. Time dependent calculations using multigrid, with applications to unsteady flows past airfoils and wings. *AIAA paper 91-1596*, AIAA 10th Computational Fluid Dynamics Conference, Honolulu, Hawaii, June 1991.
- [19] A. Jameson. Analysis and design of numerical schemes for gas dynamics 1, artificial diffusion, upwind biasing, limiters and their effect on multigrid convergence. *Int. J. of Comp. Fluid Dyn.*, 4:171-218, 1995.
- [20] A. Jameson. Analysis and design of numerical schemes for gas dynamics 2, artificial diffusion and discrete shock structure. *Int. J. of Comp. Fluid Dyn.*, To Appear.
- [21] M. Jayaram and A. Jameson. Multigrid solution of the Navier-Stokes equations for flow over wings. *AIAA paper 88-0705*, AIAA 26th Aerospace Sciences Meeting, Reno, Nevada, January 1988.
- [22] D. Johnson and L. King. A mathematically simple turbulence closure model for attached and separated turbulent boundary layers. *AIAA Journal*, 23:1684-1692, 1985.
- [23] W.P. Jones and B.E. Launder. The calculation of low-Reynolds-number phenomena with a two-equation model of turbulence. *Int. J. of Heat Tran.*, 16:1119-1130, 1973.
- [24] T.J. Kao, T.Y. Su, and N.J. Yu. Navier-Stokes calculations for transport wing-body configurations with nacelles and struts. AIAA Paper 93-2945, AIAA 24th Fluid Dynamics Conference, Orlando, July 1993.
- [25] L.D Landau and E.M. Lifshitz. *Fluid Mechanics*. Butterworth Heinemann, Oxford, 1987. II edition.
- [26] F. Liu and A. Jameson. Multigrid Navier-Stokes calculations for three-dimensional cascades. *AIAA paper 92-0190*, AIAA 30th Aerospace Sciences Meeting, Reno, Nevada, January 1992.
- [27] L. Martinelli and A. Jameson. Validation of a multigrid method for the Reynolds averaged equations. *AIAA paper 88-0414*, 1988.

- [28] L. Martinelli, A. Jameson, and E. Malfa. Numerical simulation of three-dimensional vortex flows over delta wing configurations. In M. Napolitano and F. Solbetta, editors, *Proc. 13th International Conference on Numerical Methods in Fluid Dynamics*, pages 534-538, Rome, Italy, July 1992. Springer Verlag, 1993.
- [29] F. Menter. Zonal two-equation $k-\omega$ turbulence models for aerodynamic flows. AIAA Paper 93-2906, AIAA 24th Fluid Dynamics Meeting, Orlando, July 1993.
- [30] K.W. Noonan. Aerodynamic characteristics of two rotorcraft airfoils designed for application to the inboard region of a main rotor blade. NASA-TP 3009, 1990.
- [31] H. Rieger and A. Jameson. Solution of steady three-dimensional compressible Euler and Navier-Stokes equations by an implicit LU scheme. *AIAA paper 88-0619*, AIAA 26th Aerospace Sciences Meeting, Reno, Nevada, January 1988.
- [32] P.L. Roe. Approximate Riemann solvers, parameter vectors, and difference schemes. *J. Comp. Phys.*, 43:357-372, 1981.
- [33] A. Roshko. On the development of turbulent wakes from vortex streets. *NACA Rep. 1191*, 1954.
- [34] C.L. Rumsey and V.N. Vatsa. A comparison of the predictive capabilities of several turbulence models using upwind and centered - difference computer codes. AIAA Paper 93-0192, AIAA 31st Aerospace Sciences Meeting, Reno, January 1993.
- [35] H. Schlichting. *Boundary Layer Theory*. McGraw-Hill, New York, 1979. VII-th edition.
- [36] B. R. Smith. A near wall model for the $k-l$ two equation turbulence model. *AIAA paper 94-2386*, 25th AIAA Fluid Dynamics Conference, Colorado Springs, CO, June 1994.
- [37] L.M. Smith and W.C. Reynolds. On the Yakhot-Orszag renormalization group for deriving turbulence statistics and models. *Phys. Fluids A*, 4:364-390, 1992.
- [38] P. Spalart and S. Allmaras. A one-equation turbulent model for aerodynamic flows. AIAA Paper 92-0439, AIAA 30th Aerospace Sciences Meeting, Reno, NV, January 1992.
- [39] C.G. Speziale, E.C. Anderson, and R. Abid. A critical evaluation of two-equation models for near wall turbulence. AIAA Paper 90-1481, June 1990. ICASE Report 90-46.
- [40] S. Tatsumi, L. Martinelli, and A. Jameson. Design, implementation, and validation of flux limited schemes for the solution of the compressible Navier-Stokes equations. *AIAA paper 94-0647*, AIAA 32nd Aerospace Sciences Meeting, Reno, Nevada, January 1994.
- [41] S. Tatsumi, L. Martinelli, and A. Jameson. A new high resolution scheme for compressible viscous flows with shocks. *AIAA paper 95-0466*, AIAA 33rd Aerospace Sciences Meeting, Reno, Nevada, January 1995.
- [42] D.C. Wilcox. A half a century historical review of the $k-\omega$ model. AIAA Paper 91-0615, AIAA 29th Aerospace Sciences Meeting, Reno, NV, January 1991.
- [43] C.H.K. Williamson. Defining a universal and continuous strouhal-reynolds number relationship for the laminar vortex shedding of a circular cylinder. *Phys. Fluids*, 31:2742-2744, 1988.
- [44] C.H.K. Williamson and A. Roshko. Measurements of base pressure in the wake of a cylinder at low reynolds numbers number relationship for the laminar vortex shedding. *Z. Flugwiss. Weltraumforsch.*, 14:38-46, 1990.
- [45] V. Yakhot and S.A. Orszag. Renormalization group analysis of turbulence. I. Basic theory. *J. Sci. Comp.*, 1:3-51, 1986.

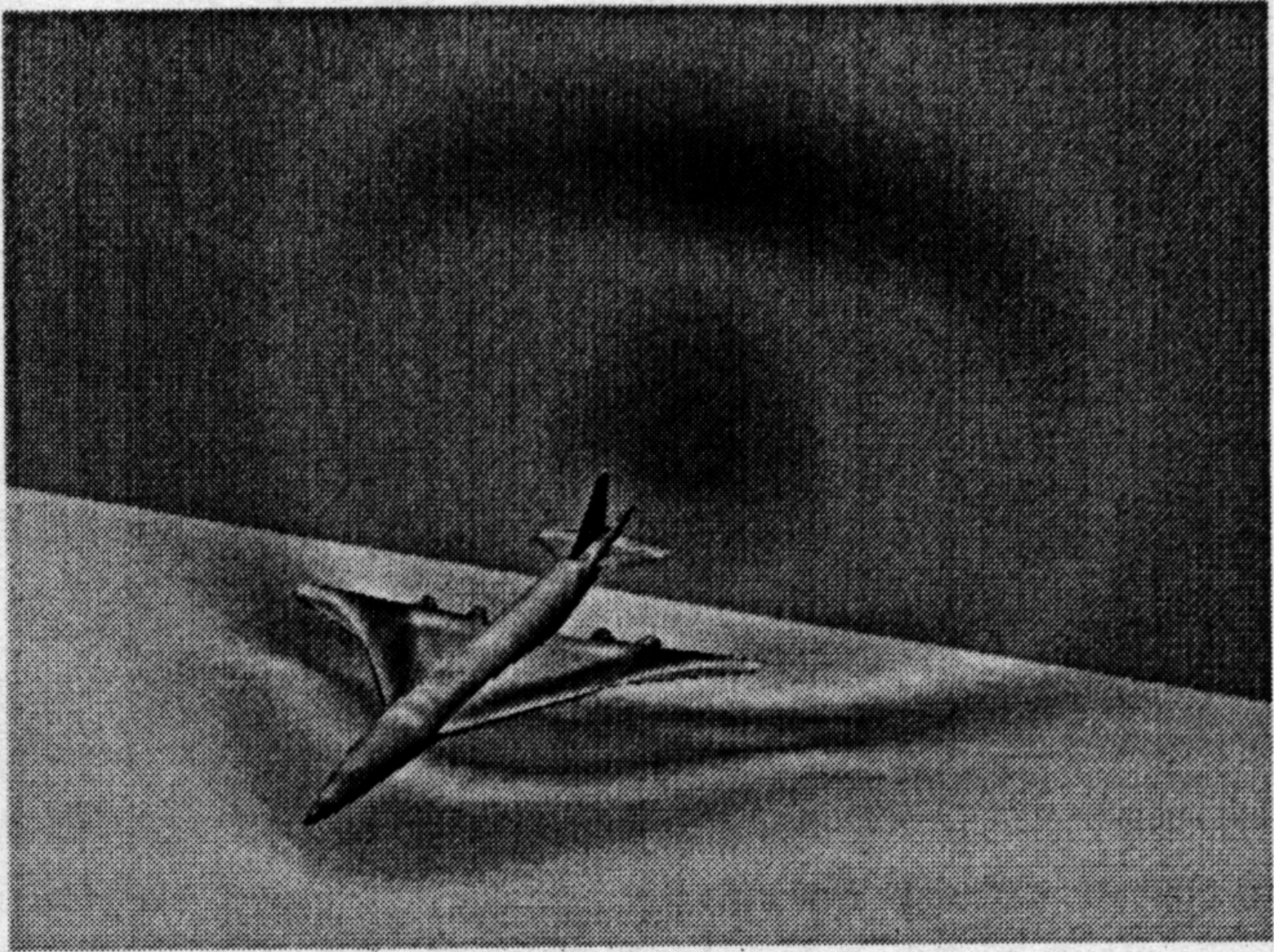


Figure 9: Pressure Contours and Sonic Boom on a Representative HSCT Configuration